Analysis of DC-Link Low-Frequency Current Harmonics in Multi-Source Multi-Three-Phase Electric Drives

Yiyu Lai, Antoine Cizeron, Adrien Voldoire, Javier Ojeda, Olivier Béthoux

To cite this version:

Yiyu Lai, Antoine Cizeron, Adrien Voldoire, Javier Ojeda, Olivier Béthoux. Analysis of DC-Link Low-Frequency Current Harmonics in Multi-Source Multi-Three-Phase Electric Drives. Electronics, 2024, 13 (12), pp.2236. 10.3390/electronics13122236 . hal-04622461

HAL Id: hal-04622461

https://hal.science/hal-04622461

Submitted on 4 Sep 2024

electronics

MDPI

Article

Analysis of DC-Link Low-Frequency Current Harmonics in Multi-Source Multi-Three-Phase Electric Drives

Yiyu Lai [1,2,3,*], Antoine Cizeron [4], Adrien Voldoire [1,2], Javier Ojeda [3] and Olivier Béthoux [1,2]

[1] Sorbonne Université, CNRS, Laboratoire de Génie Electrique et Electronique de Paris, 75005 Paris, France; olivier.bethoux@centralesupelec.fr (O.B.)
[2] Université Paris-Saclay, CentraleSupélec, CNRS, Laboratoire de Génie Electrique et Electronique de Paris, 91192 Gif-sur-Yvette, France
[3] Université Paris-Saclay, ENS Paris-Saclay, CNRS, SATIE, 91190 Gif-sur-Yvette, France; javier.ojeda@ens-paris-saclay.fr
[4] Universite Claude Bernard Lyon 1, Ampère, UMR5005, INSA Lyon, Ecole Centrale de Lyon, CNRS, 69100 Villeurbanne, France
* Correspondence: yiyu.lai@sorbonne-universite.fr

Abstract: In a multi-source permanent magnet synchronous motor (PMSM) drive, three distinct winding structures can be implemented: multi-sector, multi-three-phase, and highly coupled. However, due to variations in the magnetic coupling between windings, their low-frequency DC-link current ripple components differ. This paper presents a method to identify the phenomena associated with each low-frequency harmonic content. Three analytical models are developed for the DC current ripple induced by unbalanced winding, counter-electromotive force (back-EMF) harmonics and aliasing effects, respectively, with the results validated through simulations. Experimental validation is conducted for highly coupled winding drives, demonstrating agreement with the analytical models and simulations. The maximum DC current ripple ratio found in the analytical model, the simulation and the experiments is less than 15%, which is deemed acceptable for motor drive applications.

Keywords: multiphase drives; multi-three-phase drives; permanent magnet synchronous motors; DC-link current; current ripple; low-frequency harmonics

check for updates

Citation: Lai, Y.; Cizeron, A.;Voldoire, A.; Ojeda, J.; Béthoux, O. Analysis of DC-Link Low-Frequency Current Harmonics in Multi-Source Multi-Three-Phase Electric Drives. *Electronics* **2024**, *13*, 2236. https://doi.org/10.3390/electronics13122236

Academic Editor: Omid Beik

Received: 29 April 2024
Revised: 4 June 2024
Accepted: 5 June 2024
Published: 7 June 2024

1. Introduction

Multi-phase drive structures have gained popularity in the industry due to their additional degrees of freedom, enabling applications such as faulty operation and power sharing. Among these structures, multi-three-phase drives are particularly intriguing as they do not necessitate extensive modifications to inverter designs. Most changes are made in the electrical machine, by rearranging the stator windings. Various multi-three-phase structures can be achieved. In the case of permanent magnet synchronous motor (PMSM) drives, as illustrated in Figure 1, three main winding structures can be identified: multi-sector winding [1,2], multi-three-phase winding [3–5], and highly coupled winding [6–9]. One problem of using multi-three-phase drives is the DC-link design. For the power-sharing application and DC capacitor sizing, it is crucial to know the possible current ripple induced by the drive. The DC current ripple is responsible for decreasing the lifespan of DC capacitors [10], as well as presenting challenges in control and electromagnetic compatibility.

To study the DC current ripple, most publications utilize analytical analysis to calculate DC-link average and root mean square (RMS) expressions [11–16]. With the emergence of multi-phase drives, similar analyses have been conducted on multi-phase inverters [17,18]. Another method proposed in [19] for studying DC current ripples in three-phase inverters, and later applied to multi-phase inverters [20], is the symmetric sequence vector approach. Instead of obtaining an RMS value of current ripples, this approach permits a fine frequency analysis of the current ripple. According to [19,20] an unbalanced load for three-phase and multi-phase

DC/AC inverters results in a double-fundamental harmonic in the DC-link current, which has twice the fundamental electrical frequency. Besides the double-fundamental harmonic, the symmetric sequence approach helps analyze other low-frequency DC-link current harmonics as will be developed in this article.

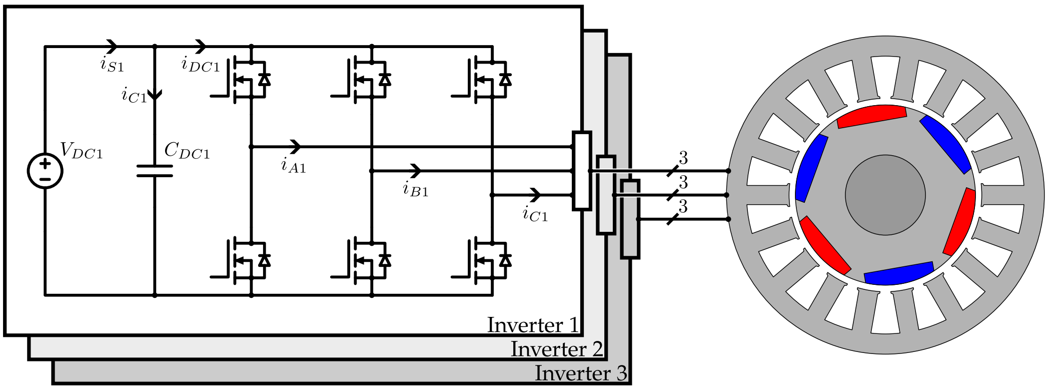

Figure 1. Multi-three-phase drive: multi-port PMSM and its three-phase DC/AC inverters.

Other DC current ripple studies take into account the DC capacitor electrical model and thermal model, which allows for calculating the capacitor core temperature increase due to current harmonics. Optimal control methods can be deduced with respect to the longest expected capacitor lifetime [21]. The capacitor type has also a great impact. For example, non-electrolytic capacitors have much lower capacitance density than electrolytic capacitors, which may cause ripples on the load side and DC voltage instability [22]. The DC-link modeling also helps to calculate DC power ripples caused by LC resonance of DC-link, and active damping control can be applied to improve these ripples [23].

While the low-frequency DC current ripple is often presumed to damage voltage sources such as lithium-ion batteries and fuel cells, recent research indicates that low-frequency ripples (ranging from 100 Hz to 1 kHz) has no adverse aging effect on lithium-ion batteries ($LiFePO_4$ and NMC/graphite prismatic) [24,25]. However, current ripples below 10 Hz can lead to an increase in capacitor impedance and result in capacitance fade [26,27], though its significance in motor drive applications is diminished due to the relatively higher electrical speed of the motor drive. Conversely, fuel cells are sensitive to current ripples, as low-frequency ripples induce detrimental effects on the proton exchange membrane fuel cell (PEMFC) lifespan [28]. Experimental findings suggest that the current ripple at 120 Hz can contribute to a 10% power reduction [29], and the low-frequency (around 100 Hz) current ripple leads to long-term degradation of fuel cells. Notably, the current ripple below 40% results in less than a 1.5% power reduction, which may be deemed acceptable. In [30], a power quality standard is proposed in order to limit stress and aging of DC-link devices. A current ripple below 10% is judged acceptable for capacitors, supercapacitors and batteries, and current ripples below 6% is judged acceptable for fuel cells.

There are various causes of the DC-link low-frequency current harmonic, but most literature investigates the harmonics on the AC side of the inverter. In [31], the effects of unbalanced windings in the PMSM are presented, and shown to result in a magnetomotive force with harmonic contents. In [32], back-EMF harmonics from magnetizing and demagnetizing in the variable flux machine cause AC current harmonics, and thus torque ripples [33]. When supplied by inverters, aliasing of switching harmonics in the control loop can also cause low-frequency harmonics. To mitigate this phenomenon, efficient filtering techniques are investigated in [34,35].

In the literature, few publications deal with the impact of unequal source contributions on low-frequency ripple. Similarly, very few works study the connection between multi-three-phase PMSM winding structures and intermediate circuit current harmonics, and even fewer publications analyze the current ripple amplitude for each harmonic order.

To address the scientific gaps described above, this paper provides three novel analytical models for low-frequency DC-link current harmonics in multi-source multi-three-phase drive applications, which are then confirmed by simulations and experiments. Recommendations are then given to reduce these low-frequency harmonics when the application requires it.

A modeling approach for winding structures of multi-three-phase PMSMs is presented in Section 2. Section 3 analyzes the DC current ripple induced by unbalanced winding. Section 4 investigates the back-EMF harmonics and their effect on the DC current harmonics. Section 5 suggests a method to quantify the current sampling issue induced by unbalanced power sharing. Simulation and experimental results are presented in Section 6. Finally, Section 7 draws conclusions and perspectives based on the analysis of the DC-link current low-frequency harmonics in multi-port motor drives.

2. Modeling and Analysis of Three Types of Multi-Port PMSM

The study of low-frequency harmonics in PMSM requires the development of analytical models. In this section, a general model based on inductance and resistance matrices is developed to be used in Sections 3–5 for each machine and for each harmonic contribution.

Figure 2 illustrates two distinct winding configurations. The difference between these two configurations is based on the arrangement of the windings around the magnetic circuit, which induces a difference in the values of the self and mutual inductances. In Figure 2a, the multi-sector (MS) winding PMSM, each of the three phases within a sub-winding is arranged within a 120° sector. The substantial separation between sub-windings minimizes the magnetic flux transfer between them. Consequently, the mutual inductance between sub-windings is negligible. Conversely, in Figure 2b, the highly coupled (HC) winding PMSM, sub-windings share the same magnetic circuit, with only marginal leakage flux present between them. Accordingly, the mutual inductance between sub-windings is close to the self-inductance of each individual sub-winding. The magnetomotive force (MMF) of the MS winding and HC winding configurations are shown in Figure 2c and Figure 2d, respectively. At the instant considered, the current in phase A is at its maximum value I while the currents in the 2 other phases B and C are $-I/2$. The total number of turns in each slot is similar, its value being named N. In this representation, the unit of MMF is normalized with respect to N and I. First, note that the evolution of the MMF induced by each MS elementary component is concentrated in its region (namely a third turn in this case), while the HC elementary component is evenly distributed on a complete circle. Second, when not constant, the elementary MS contribution is three times that of the HC one. Third, although the MMF of one sub-winding differs, the global MMF of the two segmented architectures are similar by addition.

As depicted in Figure 2, a smooth air-gap PMSM is considered.

2.1. Conventional PMSM

The general electrical model of PMSM is expressed as follows:

$$u_{abc} = [\mathcal{R}]i_{abc} + [\mathcal{L}]\frac{\mathrm{d}i_{abc}}{\mathrm{d}t} + e_{abc} \tag{1}$$

where u_{abc} represents the three-phase voltage, i_{abc} represents the three-phase current, and e_{abc} represents the back-EMF induced by the rotor:

$$\begin{aligned} u_{abc} &= (u_a, u_b, u_c)^T \\ i_{abc} &= (i_a, i_b, i_c)^T \\ e_{abc} &= (e_a, e_b, e_c)^T \end{aligned}$$

$[\mathcal{R}]$ and $[\mathcal{L}]$ are the resistance matrix and inductance matrix of multi-port PMSM winding.

$$\mathcal{L} = \begin{bmatrix} L & k_m L & k_m L \\ k_m L & L & k_m L \\ k_m L & k_m L & L \end{bmatrix} \qquad \mathcal{R} = \begin{bmatrix} R & 0 & 0 \\ 0 & R & 0 \\ 0 & 0 & R \end{bmatrix} \tag{2}$$

where k_m is the coupling factor between the three phases, $k_m L$ is the mutual inductance between the three phases.

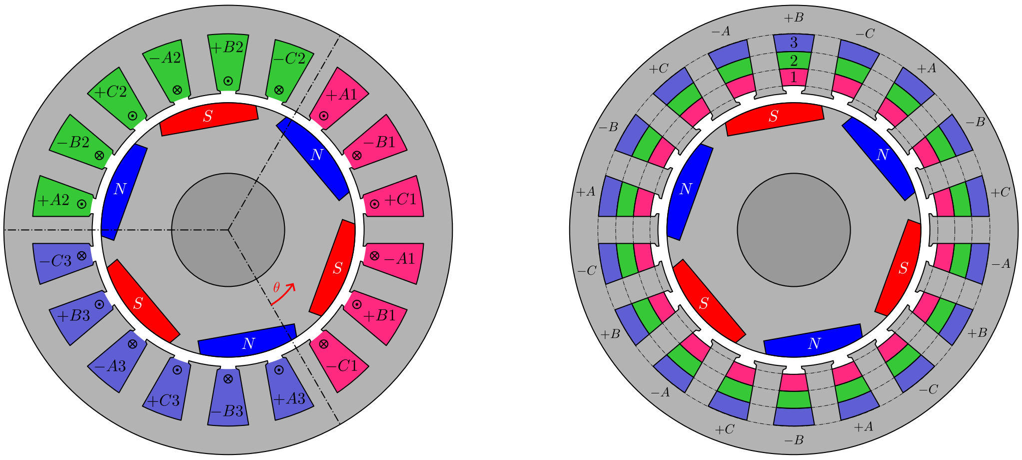

(**a**) MS winding. (**b**) HC winding.

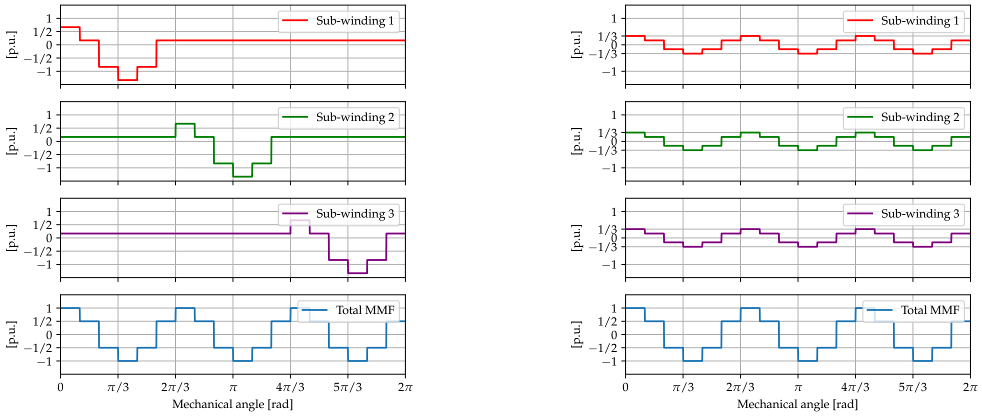

(**c**) MMF for MS configuration. (**d**) MMF for HC configuration.

Figure 2. Two multi-port PMSM winding configurations with the least coupled sub-windings (MS) and the most coupled sub-windings (HC).

2.2. Multi-Three-Phase PMSM

In a multi-three-phase PMSM, the current, voltage and back-EMF vector length is multiplied by the number of three-phase systems. Taking the example of three-port PMSM, the length of electrical vectors becomes nine:

$$\begin{aligned} u_{abc} &= (u_{a1}, u_{b1}, u_{c1}, u_{a2}, u_{b2}, u_{c2}, u_{a3}, u_{b3}, u_{c3})^T \\ i_{abc} &= (i_{a1}, i_{b1}, i_{c1}, i_{a2}, i_{b2}, i_{c2}, i_{a3}, i_{b3}, i_{c3})^T \\ e_{abc} &= (e_{a1}, e_{b1}, e_{c1}, e_{a2}, e_{b2}, e_{c2}, e_{a3}, e_{b3}, e_{c3})^T \end{aligned}$$

The resistance matrix and inductance matrix also take three times the shape than that of a normal PMSM and become 9×9 matrices. The multi-three-phase inductance matrices can be regarded as an assembly of 3×3 sub-matrices, two kinds of inductance sub-matrices are identified: $\mathcal{L}$ is the inductance matrix inside one three-phase system, and $\mathcal{N}$ is the inductance matrix between two three-phase-systems. The two sub-matrices are defined as

$$\mathcal{L} = \begin{bmatrix} L_s & k_m L_s & k_m L_s \\ k_m L_s & L_s & k_m L_s \\ k_m L_s & k_m L_s & L_s \end{bmatrix} \qquad \mathcal{N} = \begin{bmatrix} k_n L_s & k_n k_m L_s & k_n k_m L_s \\ k_n k_m L_s & k_n L_s & k_n k_m L_s \\ k_n k_m L_s & k_n k_m L_s & k_n L_s \end{bmatrix} \tag{3}$$

where k_n is the coupling factor between sub-windings, L_s is the phase self inductance of multiport PMSM. By segmenting a conventional PMSM winding into multiple subwinding, the phase self inductance decreases. Multiport winding structures are compared in the same magnetic circuit (same PMSM structure), and the following relation exists between conventional phase self inductance L and segmented phase self inductance L_s:

$$L_s = \frac{L}{3(2k_n + 1)} \tag{4}$$

By assembling the sub-matrices, the full inductance matrix of a multi-three-phase PMSM can be obtained:

$$\mathcal{L}_{3\times3\text{ph}} = \begin{bmatrix} \mathcal{L} & \mathcal{N} & \mathcal{N} \\ \mathcal{N} & \mathcal{L} & \mathcal{N} \\ \mathcal{N} & \mathcal{N} & \mathcal{L} \end{bmatrix} \tag{5}$$

The sub-winding resistance can also be represented in matrix form, where each diagonal term of the matrix corresponds to the resistance of one sub-winding.

$$\mathcal{R}_{3\times3\text{ph}} = \begin{bmatrix} \mathcal{R} & \mathcal{O}_3 & \mathcal{O}_3 \\ \mathcal{O}_3 & \mathcal{R} & \mathcal{O}_3 \\ \mathcal{O}_3 & \mathcal{O}_3 & \mathcal{R} \end{bmatrix} \quad \text{with} \quad \mathcal{R} = \begin{bmatrix} R & 0 & 0 \\ 0 & R & 0 \\ 0 & 0 & R \end{bmatrix} \tag{6}$$

where $\mathcal{O}_3$ is a 3×3 zero matrix.

The differentiation of the three multi-three-phase structures lies in the inductance sub-matrices $\mathcal{N}$, and depending on the coupling between sub-windings, $\mathcal{N}$ does not take the same value.

2.3. Control Strategy for Three-Port Three-Phase PMSM

Vectorial transformation is necessary for PMSM control, and in [36], a general method is proposed for determining the transformation matrix by constructing each line of the transformation matrix as an eigenvector of the inductance matrix. In practical applications, the generalized Clarke transformation is used to diagonalize the inductance matrix of a standard three-phase PMSM, which leads to the decoupling of the electrical vector. The inverse generalized Clarke's transformation matrix $\mathcal{P}_{\text{clarke}}^{-1}$ is defined as follows:

$$\mathcal{P}_{\text{clarke}}^{-1} = \begin{bmatrix} P_{\text{clarke}}^{-1} & \mathcal{O}_3 & \mathcal{O}_3 \\ \mathcal{O}_3 & P_{\text{clarke}}^{-1} & \mathcal{O}_3 \\ \mathcal{O}_3 & \mathcal{O}_3 & P_{\text{clarke}}^{-1} \end{bmatrix} \tag{7}$$

$$\text{with} \quad P_{\text{clarke}}^{-1} = \sqrt{\frac{2}{3}} \begin{bmatrix} \cos(\theta) & \cos(\theta - \frac{2\pi}{3}) & \cos(\theta + \frac{2\pi}{3}) \\ -\sin(\theta) & -\sin(\theta - \frac{2\pi}{3}) & -\sin(\theta + \frac{2\pi}{3}) \\ \frac{\sqrt{2}}{2} & \frac{\sqrt{2}}{2} & \frac{\sqrt{2}}{2} \end{bmatrix}$$

with $x_{abc} = \mathcal{P}_{\text{clarke}} x_{dqo}$, the electrical Equation (1) of a normal three-phase PMSM can be reformulated in the generalized Clarke frame (dqo) as

$$u_{dqo} = [\mathcal{R}_{dqo}] i_{dqo} + [\mathcal{L}_{dqo}] \frac{\mathrm{d}}{\mathrm{d}t} i_{dqo} + \omega [\mathcal{L}_{dqo}] [\mathcal{R}_{\frac{\pi}{2}}] i_{dqo} + e_{dqo} \tag{8}$$

where $[\mathcal{R}_{dqo}] = \mathcal{P}_{\text{clarke}}^{-1} [\mathcal{R}] \mathcal{P}_{\text{clarke}}$, $[\mathcal{L}_{dqo}] = \mathcal{P}_{\text{clarke}}^{-1} [\mathcal{L}] \mathcal{P}_{\text{clarke}}$. And $[\mathcal{R}_{\frac{\pi}{2}}]$ is the 3D rotation matrix on the d–q plane, representing a $\pi/2$ anti-clockwise rotation:

$$[\mathcal{R}_{\frac{\pi}{2}}] = \begin{bmatrix} R_{\frac{\pi}{2}} & \mathcal{O}_3 & \mathcal{O}_3 \\ \mathcal{O}_3 & R_{\frac{\pi}{2}} & \mathcal{O}_3 \\ \mathcal{O}_3 & \mathcal{O}_3 & R_{\frac{\pi}{2}} \end{bmatrix} \quad \text{with} \quad [R_{\frac{\pi}{2}}] = \begin{bmatrix} 0 & -1 & 0 \\ 1 & 0 & 0 \\ 0 & 0 & 0 \end{bmatrix} \tag{9}$$

However, in the specific case of a multi-three-phase PMSM, an additional transformation is required to diagonalize the $\mathcal{L}_{3\times3\text{ph}}$ if the coupling factor k_n is significant [37,38]. In [7], a common and differential mode transformation $\mathcal{P}_{\Sigma\delta}$ is proposed.

$$\mathcal{P}_{\Sigma\delta}^{-1} = \begin{bmatrix} \mathcal{I}_3 & \mathcal{I}_3 & \mathcal{I}_3 \\ \mathcal{I}_3 & -\mathcal{I}_3 & \mathcal{O}_3 \\ \mathcal{O}_3 & \mathcal{I}_3 & -\mathcal{I}_3 \end{bmatrix} \tag{10}$$

where $\mathcal{I}_3$ is a 3×3 identity matrix.

The electrical vectors in $\Sigma\delta$ frame is written as follows:

$$\begin{aligned} u_{\Sigma\delta} &= (\Sigma u_d, \Sigma u_q, \Sigma u_o, \delta_{12}u_d, \delta_{12}u_q, \delta_{12}u_o, \delta_{23}u_d, \delta_{23}u_q, \delta_{23}u_o)^T \\ i_{\Sigma\delta} &= (\Sigma i_d, \Sigma i_q, \Sigma i_o, \delta_{12}i_d, \delta_{12}i_q, \delta_{12}i_o, \delta_{23}i_d, \delta_{23}i_q, \delta_{23}i_o)^T \\ e_{\Sigma\delta} &= (\Sigma e_d, \Sigma e_q, \Sigma e_o, \delta_{12}e_d, \delta_{12}e_q, \delta_{12}e_o, \delta_{23}e_d, \delta_{23}e_q, \delta_{23}e_o)^T \end{aligned}$$

The Σ currents represent the sum of three sub-winding currents, and the δ_{12} currents represent the current difference between sub-winding 1 and sub-winding 2, and the δ_{23} currents represent the current difference between sub-winding 2 and sub-winding 3.

In normal operating conditions, the current vector i_q is intentionally aligned to the back-EMF vector to achieve the maximum mechanical output of the PMSM, the Σi_q current is directly proportional to the mechanical torque of the multi-port PMSM (self-control).

Applying the $\Sigma\delta$ transformation on the dq-frame equation (Equation (8)), the $\Sigma\delta$-frame equation is written as follows:

$$u_{\Sigma\delta} = [\mathcal{R}_{\Sigma\delta}]i_{\Sigma\delta} + [\mathcal{L}_{\Sigma\delta}]\frac{\mathrm{d}}{\mathrm{d}t}i_{\Sigma\delta} + \omega[\mathcal{L}_{\Sigma\delta}][\mathcal{R}_{\frac{\pi}{2}}]i_{\Sigma\delta} + e_{\Sigma\delta} \tag{11}$$

where $[\mathcal{R}_{\Sigma\delta}] = \mathcal{P}_{\Sigma\delta}^{-1}[\mathcal{R}_{dqo}]\mathcal{P}_{\Sigma\delta}$, $[\mathcal{L}_{\Sigma\delta}] = \mathcal{P}_{\Sigma\delta}^{-1}[\mathcal{L}_{dqo}]\mathcal{P}_{\Sigma\delta}$.

The inductance and resistance matrices in $\Sigma\delta$ frame are presented in Table 1, since the inductance matrix is diagonalized after two transformations, only diagonal values are presented. It can be found that the Σ inductance is the same as the δ inductance when $k_n = 0$. However, in the HC case, $1 - k_n$ is very close to zero, meaning that the δ inductance is very close to 0.

Table 1. Resistances and inductances in the $\Sigma\delta$ frame.

Axis	Resistance	Inductance
Σ_d, Σ_q	R	$\frac{1-k_m}{3}L$
Σ_o	R	$\frac{1+2k_m}{3}L$
δ_{12d}, δ_{12d} δ_{12d}, δ_{12d}	R	$\frac{(1-k_m)(1-k_n)}{3(1+2k_n)}L$
δ_{12o}, δ_{23o}	R	$\frac{(1+2k_m)(1-k_n)}{3(1+2k_n)}L$

The control scheme for three types of multi-port PMSMs is set to be the same (see Figure 3): the control reference is made in the $\Sigma\delta$ space. Since the generalized Clarke transformation is performed before the $\Sigma\delta$ transformation, the reference is a DC value. The $\Sigma\delta$ transformation makes the control more adapted to the physical structure: the Σ reference represents the total contribution of the three DC sources, while the δ references denote the contribution difference between each pair of sources (δ_{12} and δ_{23}). As discussed in the previous section, two transformations are necessary for HC windings PMSM in order to completely decouple the controlled axes. Conversely, only one transformation is sufficient to decouple the MS winding PMSM [37–39]. Figure 3 also depicts other elements in the multipoint control unit (MCU): an Analog-to-Digital converter (ADC) for phase current measurement, sampling at a specific frequency. The electrical angle measurement is accomplished by a synchro resolver on the rotor shaft, and the angle measurement is used by the generalized Clarke transform to ensure self-control condition. A symmetrical sinusoidal pulse width modulation (SPWM) is chosen due to its simple implementation and fewer high-frequency harmonics [40]. Three independent voltage sources are electrically coupled with the three sub-windings of the multi-port PMSM, where the voltage source represents an energy storage unit (e.g., battery and fuel cell). Each three-phase DC/AC voltage source inverter is equipped with six switches and one decoupling capacitor. The high-side and low-side switches are controlled with complementary signals.

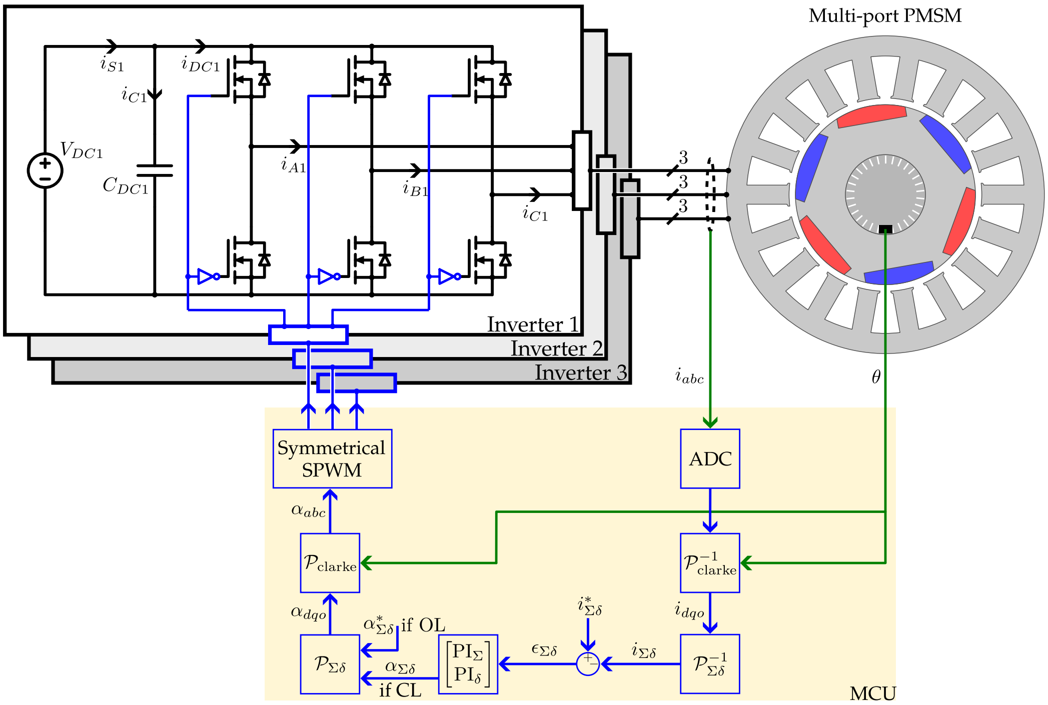

Figure 3. Control structure of multi-port PMSM considered in this study.

The analytical models proposed in Section 3–5 are in open-loop (OL) control condition. To achieve open-loop control with the desired operation point (with desired phase currents), the system is first controlled in closed-loop (CL), and once the system is stabilized at the desired operation point ($i^{*}_{\Sigma\delta}$), the average reference signal ($\alpha^{*}_{\Sigma\delta}$) is saved to then control the system in open-loop.

2.4. Standard Model for Multi-Port PMSM

Reference values for winding resistance and inductance are considered in this article, obtained from averaged measurement value of a HC PMSM platform [7,8]. Since the three multi-port winding structures have exactly the same number of turns per phase per sub-winding, the same phase resistance value is assumed for all three winding structures. The phase self inductance L_s is calculated from Equation (4) with respect to conventional three phase winding self inductance L. Table 2 shows the considered resistance and inductance values, as well as the respective coupling factor of the three winding configurations.

In the MS winding, where sub-windings are separated into 120° sectors, making the coupling factor smallest among the three structures, it is assumed that $k_n = 0$ in this case. In the HC winding, k_n is close to 1, and the measurement shows $k_n = 0.95$. Then there is multi-three-phase (P-3ph) winding with an intermediate coupling factor, let us take $k_n = 0.5$ for this case.

Table 2. Standard model value for the studied multi-port PMSM.

Parameters	**Value**		
R	345 mΩ		
L	3454 µH		
k_m	−0.3		
Winding **Parameters**	**MS**	**P-3ph**	**HC**
k_n	0	0.5	0.95

3. Analysis of Unbalanced Winding Issues

The winding unbalance may occur when the manufacturing process is not perfect or when the coil head has different lengths due to a specific spatial arrangement of inverters and PMSM.

The unbalance considered in this section is obtained from the HC PMSM platform measurement. In this particular achievement, it is found that the distance Δ between an R or L value and the average value is below 12%. This maximum distance is considered in the following analysis.

3.1. DC Current Ripple Calculation Using Admittance Approach

The multi-port PMSM is modeled by resistances and coupled inductors in series, and represented analytically as a resistance matrix and an inductance matrix. The back-EMF is not modeled in this section because the unbalanced winding analysis is normalized with respect to the supply voltage. By combining the two matrices in complex form, the admittance matrix can be expressed as

$$\mathcal{Y} = (\mathcal{R} + j\omega\mathcal{L})^{-1} \tag{12}$$

Without taking into account the back-EMF, the phase current is obtained by the following expression:

$$i_{ph} = \mathcal{Y} v_{ph} \tag{13}$$

In the case where neutral point is not connected to the DC-link middle point, to obtain the load phase voltage, the load neutral point voltage v_{nz} must be determined (Figure 4). In the case of a multi-port PMSM, the admittance matrix is not diagonal, a generalization of Millman's theorem is necessary for electrical machine neutral point voltage calculation.

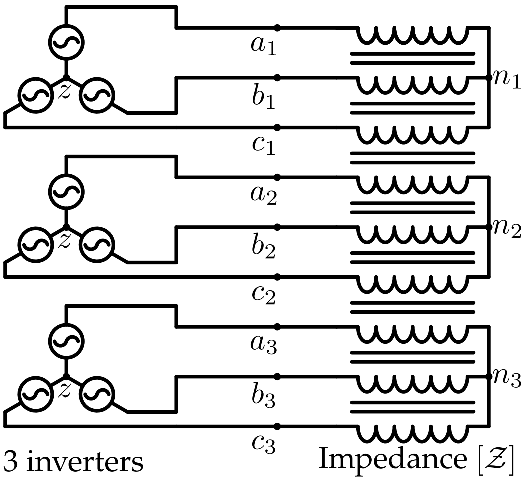

Figure 4. DC/AC inverter supply of a three-port PMSM.

From Kirchoff's voltage law,

$$v_{phz} - [\mathcal{F}_{93}]v_{nz} = [\mathcal{Z}]i_{ph} \tag{14}$$

From Kirchoff's current law,

$$[\mathcal{F}_{39}]i_{ph} = [\mathcal{O}_{31}] \tag{15}$$

with vector definitions as follows:

$$\begin{aligned} v_{phz} &= (v_{a1z}, v_{b1z}, v_{c1z}, v_{a2z}, v_{b2z}, v_{c2z}, v_{a3z}, v_{b3z}, v_{c3z})^T \\ &= V_r(\mathrm{e}^{i0}, \mathrm{e}^{i\frac{-2\pi}{3}}, \mathrm{e}^{i\frac{-4\pi}{3}}, \mathrm{e}^{i0}, \mathrm{e}^{i\frac{-2\pi}{3}}, \mathrm{e}^{i\frac{-4\pi}{3}}, \mathrm{e}^{i0}, \mathrm{e}^{i\frac{-2\pi}{3}}, \mathrm{e}^{i\frac{-4\pi}{3}})^T \end{aligned}$$

$$v_{nz} = (v_{n1z}, v_{n2z}, v_{n3z})^T$$

v_{phz} is the reference three-phase voltage supply in open-loop condition, the reference voltage takes the magnitude of V_r.

The three neutral point voltage with respect to the DC-link middle point z is then deduced using the generalized Millman's theorem:

$$v_{nz} = ([\mathcal{F}_{39}][\mathcal{Y}][\mathcal{F}_{93}])^{-1}[\mathcal{F}_{39}][\mathcal{Y}]v_{phz} \tag{16}$$

where matrix definitions are as follows:

$$[\mathcal{F}_{93}] = \begin{bmatrix} 1 & 0 & 0 \\ 1 & 0 & 0 \\ 1 & 0 & 0 \\ 0 & 1 & 0 \\ 0 & 1 & 0 \\ 0 & 1 & 0 \\ 0 & 0 & 1 \\ 0 & 0 & 1 \\ 0 & 0 & 1 \end{bmatrix} \quad [\mathcal{F}_{39}] = \begin{bmatrix} 1 & 1 & 1 & 0 & 0 & 0 & 0 & 0 & 0 \\ 0 & 0 & 0 & 1 & 1 & 1 & 0 & 0 & 0 \\ 0 & 0 & 0 & 0 & 0 & 0 & 1 & 1 & 1 \end{bmatrix} \quad [\mathcal{O}_{31}] = \begin{bmatrix} 0 \\ 0 \\ 0 \end{bmatrix}$$

With v_{nz}, Equation (13) can be written into

$$\begin{aligned} i_{ph} &= \mathcal{Y}(v_{phz} - v_{nz}) \\ &= \mathcal{Y}\Big(v_{phz} - ([\mathcal{F}_{39}][\mathcal{Y}][\mathcal{F}_{93}])^{-1}[\mathcal{F}_{39}][\mathcal{Y}]v_{phz}\Big) \end{aligned} \tag{17}$$

Then, for each unbalanced admittance matrix, the current vector i_{ph} can be calculated.

From Appendix A, it is shown that the DC component of DC-link current is proportional to the multiplication of sequence 1 current magnitude and cosine of sequence 1 current phase, and the twice fundamental frequency ($2f$) current ripple component is proportional to the magnitude of sequence 2 current. To determine the DC current quality, a current ripple ratio (CRR) is defined as the ratio between the ripple magnitude and the DC current value, the maximum CRR is considered for the three inverter DC-links:

$$\mathrm{CRR}_{2f} = \max_{i \in \{1,2,3\}} \left(\frac{|\underline{I_2}|}{|\underline{I_1}| \cos \angle \underline{I_1}} \right)_i \tag{18}$$

3.2. Unbalance Scenarios in Multiport PMSM

Some standard unbalance cases can be defined, with all other types of unbalance regarded as a superposition of several standard cases. The unbalance scenarios considered are explained in Table 3.

Table 3. Considered resistance and inductance unbalance scenarios in multi-port winding.

Scenario	Modeling Details
1ph R	ΔR is added to phase A of all three sub-windings
1sub 1ph R	ΔR is added to phase A of the first sub-winding
1ph L	ΔL is added to phase A self inductance of all three sub-windings
1sub 1ph L	ΔL is added to phase A self inductance of the first sub-winding
all M	$\Delta k_m L$ or $\Delta k_n k_m L$ is added to the mutual inductance between every phase A and every phase C
inter-sub M	$\Delta k_n k_m L$ is added to the mutual inductance between phase A and phase C between sub-winding 1 and sub-winding 3

In Figure 5, the current ripple ratio results are presented at the rated frequency 200 Hz, and the results are obtained with the standard model value, with a variation of the Δ value within $[-12\%, 12\%]$. The results show that the HC winding is the most sensitive configuration to winding unbalance, and the CRR is found to increase with the inter sub-winding coupling factor. In Figure 5a, there are fewer unbalance scenarios for the MS winding, because the MS winding is assumed to have no mutual inductance between sub-windings.

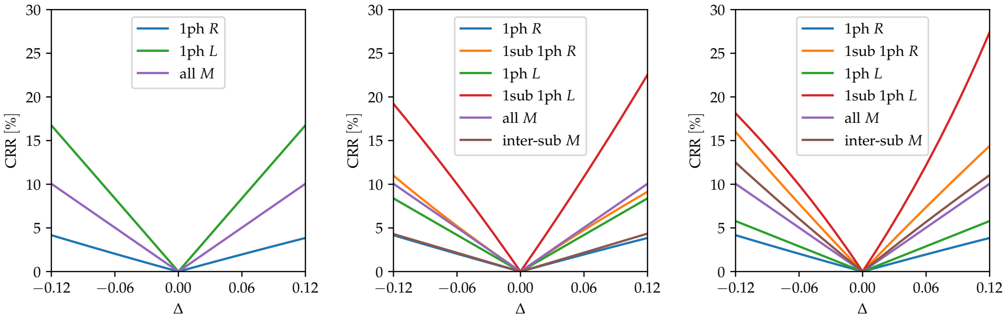

(**a**) MS winding (**b**) P-3ph winding (**c**) HC winding

Figure 5. DC-link current ripple ratio for three types of multi-port winding configuration.

3.3. Simulation Results

Simulations are carried out to confirm the DC-current ripple component (Figure 6) on PLECS. Simulation parameters are shown in Table 4. The analytical model of the $2f$ DC current harmonic is in the open-loop condition, where the voltage reference is perfectly sinusoidal. While in the simulation, the system must be first controlled in closed-loop to achieve the operation point of $\Sigma i_q = 18\,A$. Secondly, the control loop is opened by keeping the average reference in $\Sigma\delta$ frame, so that the operation point remains the same in open-loop.

Table 4. Simulation and experimental parameters.

Source	Inverter	PMSM	Control		
V_{DC}	Switching frequency	Electrical speed	PWM	PI controller	Sampling frequency
48 V	20 kHz	200 Hz	SPWM	Σ axis : $K_p = 0.165$, $K_i = 25$ δ axis : $K_p = 0.0022$, $K_i = 26$	20 kHz

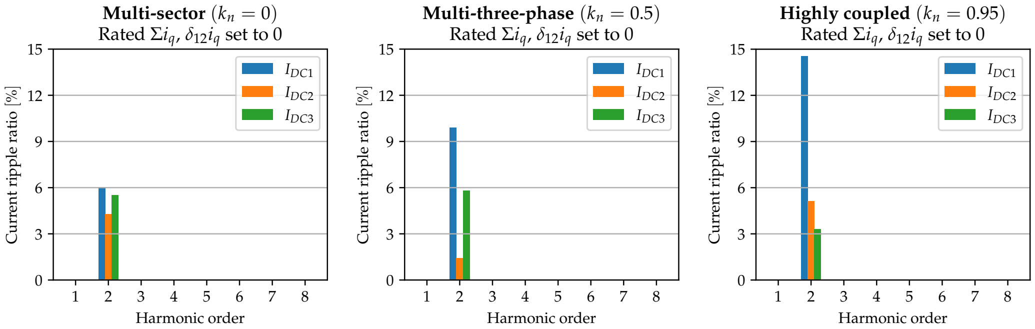

Figure 6. Open-loop simulation results with the measured winding resistance, measured inductance and ideal back-EMF. Rated Σi_q at 18 A, average DC current at 2.7 A.

No low-frequency harmonics can be observed in the ideal RL case. In Figure 6, simulation results with measured RL are presented, the harmonic at $2f$ appears. Globally, the maximum $2f$ harmonic magnitude follows the analytical analysis, it increases with the inter-sub-winding coupling factor k_n, which makes the HC winding the structure with the worst $2f$ DC current harmonic. The actual admittance model is not able to explain why the current ripple ratio increase with the coupling factor, but a hypothesis is the little δ axis inductance makes HC winding more sensitive to RL unbalance.

From simulation results in Figure 6, it can be found that in all three windings, the average current ripple ratio is around 5%. In MS winding, current ripple ratio is around 5%. In P-3ph winding, current ripple ratio is smaller than 10%. In HC winding case, the current ripple ratio is smaller than 12%. Based on analytical model results shown in Figure 5, the impact of conventional three-phase unbalance is lower for more coupled windings, while the impact of inter-sub-winding unbalance increases with the inter-sub-winding coupling factor k_n.

4. Analysis of Back-EMF Harmonic Impact

The $2f$ current harmonic is not the only low-frequency current harmonic that appears in PMSM drives' DC-link. Due to stator structure and winding configuration, the back-EMF is not perfectly sinusoidal [36]. By measuring the back-EMF of the studied machine, the fifth and seventh harmonics are the most significant harmonics found in addition to the fundamental.

4.1. DC Current Ripple Calculation Using Σ Equivalent Model

Equation (19) gives the analytical form of the fundamental and the fifth and seventh harmonics in the measured back-EMF. It can be seen that the fifth harmonic is a sequence 2 component and the seventh harmonic is a sequence 1 component. ϕ_{e1}, ϕ_{e5} and ϕ_{e7} are the phase differences between equivalent voltage vector $\underline{V}$ and equivalent back-EMF vector $\underline{E}$ of fundamental, fifth harmonic and seventh harmonic, respectively (Figure 7).

$$\begin{cases} e_a = E_{h1}\sin(\theta-\phi_{e1}) + E_{h5}\sin(5\theta-\phi_{e5}) + E_{h7}\sin(7\theta-\phi_{e7}) \\ e_b = E_{h1}\sin\left(\theta-\phi_{e1}-\dfrac{2\pi}{3}\right) + E_{h5}\sin\left(5\theta-\phi_{e5}-\dfrac{4\pi}{3}\right) + E_{h7}\sin\left(7\theta-\phi_{e7}-\dfrac{2\pi}{3}\right) \\ e_c = E_{h1}\sin\left(\theta-\phi_{e1}-\dfrac{4\pi}{3}\right) + E_{h5}\sin\left(5\theta-\phi_{e5}-\dfrac{2\pi}{3}\right) + E_{h7}\sin\left(7\theta-\phi_{e7}-\dfrac{4\pi}{3}\right) \end{cases} \quad (19)$$

The measured magnitudes of three back-EMF harmonics at 200 Hz are as follows:

- $E_{h1} = 11.84\ V$.
- $E_{h5} = 0.21\ V$.
- $E_{h7} = 0.48\ V$.

The following phase relationships are also obtained from measurement:

- $\phi_{e5} = \phi_{e1}$.
- $\phi_{e7} = \phi_{e1} + \pi$.

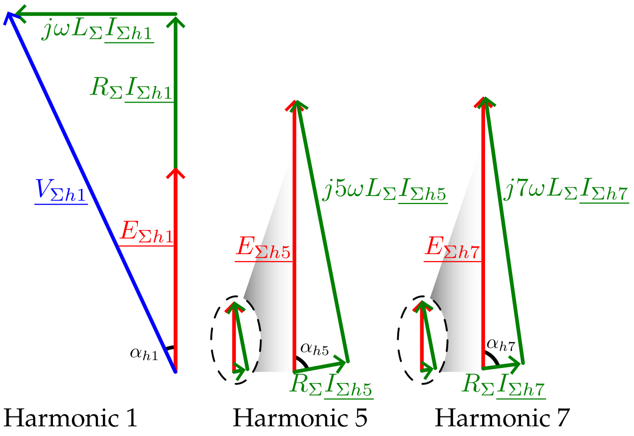

Figure 7. Vector representation of phase voltage $\underline{V}$, phase current $\underline{I}$ and back-EMF $\underline{E}$. $\underline{V}$, $\underline{I}$ and $\underline{E}$ are equivalent vectors which take Σ_q axis values, the resistance and inductance also take Σ_q axis values (Table 1).

Figure 7 illustrates a vector representation of $\underline{V}$, $\underline{I}$, and $\underline{E}$. The figure only represents components of the same frequency (the fundamental harmonic on the left and the fifth harmonic/seventh harmonic on the right). At base frequency, the back-EMF vector is in phase with the phase current vector, and the phase voltage vector equals the vectorial sum of the back-EMF vector, the resistance voltage vector, and the inductance voltage vector. At the frequency of five/seven times fundamental frequency ($5f$ or $7f$), the voltage vector does not exist in open-loop condition. Therefore, the back-EMF vector is directly the vectorial sum of the resistance voltage and the inductance voltage.

The angle α between the phase current vector and the phase voltage vector defines the system power factor. Once the inductance and resistance values are known, the angles α_{h5} and α_{h7} become constant for one electrical speed ω: $\alpha_{h5} = \arctan(5\omega L/R)$ and $\alpha_{h7} = \arctan(7\omega L/R)$. Therefore, by knowing the magnitude of the fifth and seventh back-EMF harmonics, the first, fifth, and seventh harmonics of the phase current can be calculated in the following form:

$$\begin{cases} \left|\underline{I_{\Sigma h1}}\right| = \dfrac{\left|\underline{V_{\Sigma h1}}\right| \cos\alpha_{h1} - \left|\underline{E_{\Sigma h1}}\right|}{R_\Sigma} \\ \left|\underline{I_{\Sigma h5}}\right| = \dfrac{\left|\underline{E_{\Sigma h5}}\right| \cos\alpha_{h5}}{R_\Sigma} \\ \left|\underline{I_{\Sigma h7}}\right| = \dfrac{\left|\underline{E_{\Sigma h7}}\right| \cos\alpha_{h7}}{R_\Sigma} \end{cases} \tag{20}$$

The same analysis as in Appendix A can be conducted. From the back-EMF expression in Equation (19), the fifth harmonic only has the sequence 2 component, while the seventh harmonic only has the sequence 1 component. Consequently, the current's fifth harmonic has only sequence 2 component and the current's seventh harmonic has only sequence 1 component due to proportionality between back-EMF harmonic and current harmonic. The Σ current under measured back-EMF condition can be expressed as follows:

$$I_\Sigma = \left|\underline{I_{\Sigma h1}}\right| \sin(\theta - \alpha_{h1}) + \left|\underline{I_{\Sigma h5}}\right| \sin(5\theta - 5\alpha_{h1} - \alpha_{h5}) + \left|\underline{I_{\Sigma h7}}\right| \sin(7\theta + \pi - 7\alpha_{h1} - \alpha_{h7}) \tag{21}$$

It is noteworthy that the magnitude of Σ vector is three times the magnitude of natural frame vector and that all phase angles are with respect to the open-loop phase voltage of phase A.

Finally, the expression of the DC current taking into account back-EMF harmonics can be derived from the DC average current calculation in Appendix A:

$$\begin{aligned} I_{DC,\mathrm{EMF}} = {} & \frac{D\left(\left|\underline{V_{\Sigma h1}}\right| \cos\alpha_{h1} - \left|\underline{E_{\Sigma h1}}\right|\right)\cos\alpha_{h1}}{4R_\Sigma} \\ & + \frac{D}{4R_\Sigma}\Big[-\left|\underline{E_{\Sigma h5}}\right| \cos\alpha_{h5}\cos(6\theta - 5\alpha_{h1} - \alpha_{h5}) \\ & + \left|\underline{E_{\Sigma h7}}\right| \cos\alpha_{h7}\cos(6\theta + \pi - 7\alpha_{h1} - \alpha_{h7})\Big] \end{aligned} \tag{22}$$

CRR for back-EMF induced DC current harmonics can be defined as the magnitude ratio of six times fundamental frequency ($6f$) component and DC component in Equation (22). This analytical model can give the CRR of three types of windings at the same operation point ($\overline{I_{DC}} = 2.61A$): all three structures take the same DC current ripple ratio at $6f$ at 0.995% in the measured back-EMF condition.

4.2. Simulation Results

Simulations in this section are also in open-loop condition, using the same closed-loop to open-loop method to keep the operation point (Figure 3).

Simulation results show that the measured back-EMF produces the harmonic $6f$ in the DC-link current at rated Σi_q and a DC average current of 2.61 A, the current ripple ratio of harmonic $6f$ is 0.988%. The simulation results support the demonstrations made in Section 4.1: the fifth harmonic and the seventh harmonic in back-EMF result in sixth harmonic in DC current. However, all three winding structures exhibit the same $6f$ DC current harmonic magnitude.

Comparing simulation results and analytical results in Section 4.1, a strong agreement can be found, which confirms the equal impact of back-EMF on induced DC current ripple for three winding configurations.

5. Sampling Effect on DC-Link Current Ripple

Sampling is a mandatory function in a signal processing chain dedicated to closed-loop control. Since microcontrollers used in embedded systems only accept digital signals, processing of current sensor data is necessary via an ADC. However, since the PMSM is powered by a DC/AC inverter, an ADC would take into account the high-frequency current ripple due to switching. By choosing the sampling moment properly with respect to the switching period, the current ripple could be eliminated in conventional PMSMs. However, in the case of P-3ph PMSMs and HC PMSMs, this technique does not work and the control loop cannot avoid sampling the current switching ripples that occur.

Simulations are conducted with the same switching and sampling frequency at 20 kHz, so that the sampling moment can be synchronized with the peak of the triangular carrier.

5.1. Impact of Structure on Sampling

In Figure 8, a comparison is made between HC PMSM without and with δ control. Figure 8a depicts the scenario where only the Σ reference is applied ($\Sigma i_q = 18\ A$), resulting in zero high-frequency current ripple every half switching period at the carrier's positive and negative peaks. In Figure 8b, both Σ and δ references are applied. Due to the coupling between sub-windings, the current ripple can no longer return to zero every half switching period. The ADC takes the current switching ripple into account, and the ripple value is fed back to the current controller, resulting in unwanted harmonics in the current response. This is the phenomenon of spectral aliasing.

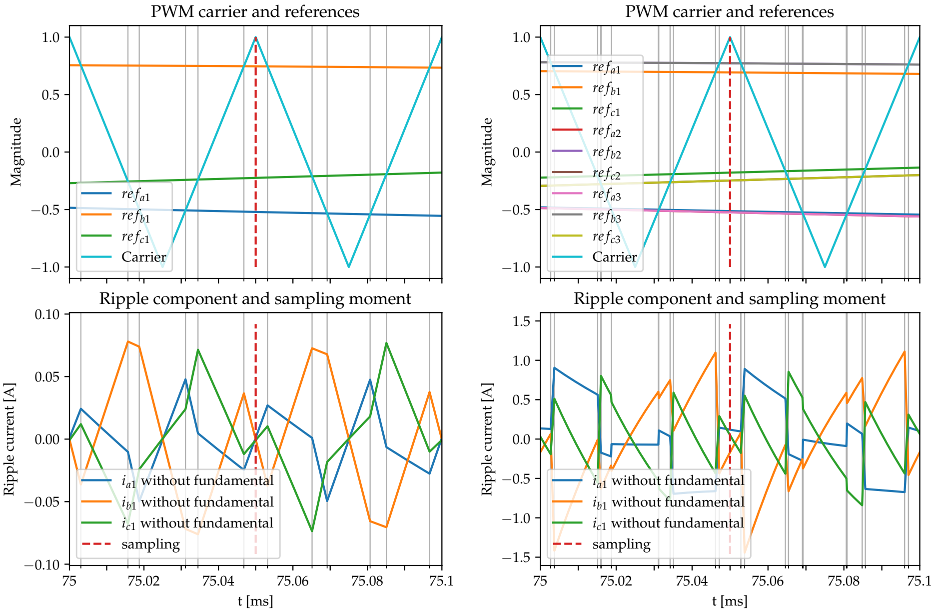

(**a**) HC PMSM with δ references set to 0. (**b**) HC PMSM with non-zero δ references.

Figure 8. Current ripple components and sampling moment of a HC winding with 0 and non-zero delta references.

5.2. Current Harmonics Induced by PWM Power Supply

The high-frequency current ripples are induced by PWM power supply of three-phase DC/AC inverters. It is necessary to investigate the harmonic components of the PWM voltage supply to understand the current ripple component (Appendix B).

As illustrated in Section 2, two transformations are applied to achieve system control decoupling. In the $\Sigma\delta$ frame where the system is decoupled, simple transfer functions can be used to approximate the relation between phase voltage and phase current (Figure 9). G_Σ and G_δ vary from three winding configurations, for MS winding $G_\Sigma = G_\delta$, but for the two other configurations, this relation is not verified. If no δ control is given (three sub-windings contribute equally), then $v_\delta = 0$, otherwise $v_\delta \neq 0$.

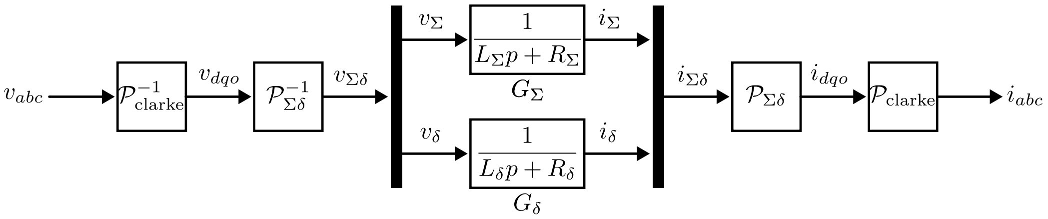

Figure 9. Transfer between phase voltage and phase current.

It is worth noting that the generalized Clarke transformation changes the harmonic order and its magnitude (Equation (7)). Equation (A9) represents the PWM voltage fundamental component and the sideband harmonics in positive angular speed, so the inverse Clarke transformation $\mathcal{P}_{\text{clarke}}^{-1}$ applies -1 to every harmonic order and a gain of $\sqrt{6}/2$ to every harmonic magnitude. Similarly, the Clarke transformation $\mathcal{P}_{\text{clarke}}$ causes $+1$ to harmonic order and apply a gain of $\sqrt{6}/3$.

Figure 10 shows the PWM voltage harmonics in dq frame v_{dqo}. Here, the maximum magnitude of phase voltage fundamental component is normalized to 1, and taking into account real inverter constraints, the modulation depth is set to 0.8, which means the fundamental component takes a magnitude of 0.8. Since the harmonic order of the fundamental component is reduced to 0 due to the inverse Clarke transformation $\mathcal{P}_{\text{clarke}}^{-1}$, the fundamental component is not shown in this figure. On the secondary axis, the bode gain plot (G_Σ and G_δ) of MS and HC winding is illustrated, representing two extreme cases of the coupling factor:

- MS: $L_\Sigma = L_\delta = (1 - k_m)L/3$, around -40 dB of attenuation on both axes at harmonic 100.
- HC: $L_\Sigma = (1 - k_m)L/3$, around -50 dB of attenuation on the Σ axis at harmonic 100; L_δ close to 0, around -10 dB of attenuation on the δ axis at harmonic 100.

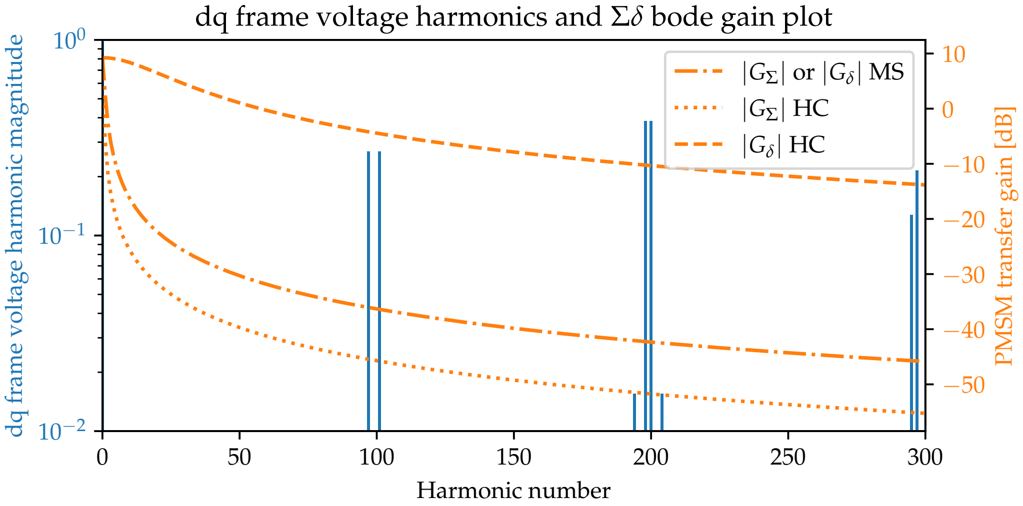

Figure 10. Clarke's frame voltage v_{dqo} harmonics and $\Sigma\delta$ frame transfer function gain.

Apparently, compared to the attenuation of Σ axis, the δ axis attenuation of HC structure is much lower and may result in residual PWM harmonics in phase current if δ mode is activated for HC structure. Since HC δ mode is the worst case when it comes to residual current harmonic, let it be the object of study in the following analysis.

The comparison in Figure 10 is made between the phase voltage in Clarke's frame and the transfer function in the $\Sigma\delta$ frame. This is an intentional choice because the Σ and δ voltage magnitude depends on the control reference. By making this comparison, equal magnitude of Σ and δ voltage is assumed.

By multiplying the transfer gain of G_δ and the Clarke frame voltage harmonic magnitude, the Clarke frame current harmonic magnitude is obtained, then using the generalized Clarke transformation, the current harmonics in natural frame are obtained. In Figure 11, the phase current harmonics composition before sampling is illustrated in blue(fundamental component) and orange(sideband harmonics). If the ADC samples the current measurement at a frequency of $f_{samp} = 100 f_e$, which is the actual experimental setting, the bandwidth of the ADC is $[-f_{samp}/2, f_{samp}/2]$. All harmonics outside the bandwidth are aliased into the bandwidth with their magnitude conserved. A detailed explanation of this phenomenon is given in Section 5.3.

5.3. Aliasing Effect of the Current Measurement

s_1 and s_2 are two signals with respective frequencies of f_1 and f_2:

$$\begin{cases} s_1 = A\sin(2\pi f_1 t + \phi) \\ s_2 = A\sin(2\pi f_2 t + \phi) \end{cases} \tag{23}$$

Their sampled signals can be exactly the same if the following relation is verified:

$$f_1 - f_2 = n f_{samp} \qquad \text{with } n \in \mathbb{Z} \tag{24}$$

where f_{samp} is the sampling frequency of the ADC, and n belongs to the set of integer $\mathbb{Z}$.

In Figure 11, it is obvious that, even in the case of HC winding configuration with δ control, the most dominant current harmonic is the first group. The following demonstration only considers the first harmonic group since it is the most significant one. The magnitude of aliased harmonics is conserved, but the frequency is aliased into the bandwidth of the ADC ($[-f_{samp}/2, f_{samp}/2]$) by adding the integer multiple of sampling frequency. Only the spectrum outside the bandwidth can be aliased into the bandwidth conserving its magnitude, and in Figure 11 the aliasing zone is marked with a gray background. The sampling frequency is the same as the first harmonic frequency (at harmonic number 100), and subtracting the first group with f_{samp} results in the aliased harmonics (in green). A negative frequency aliased harmonic at $-2f_e$ is produced that corresponds to harmonic $f_{sw} - 2f_e$ before sampling; similarly, the positive frequency aliased harmonic at $2f_e$ is from the harmonic $f_{sw} + 2f_e$ before sampling.

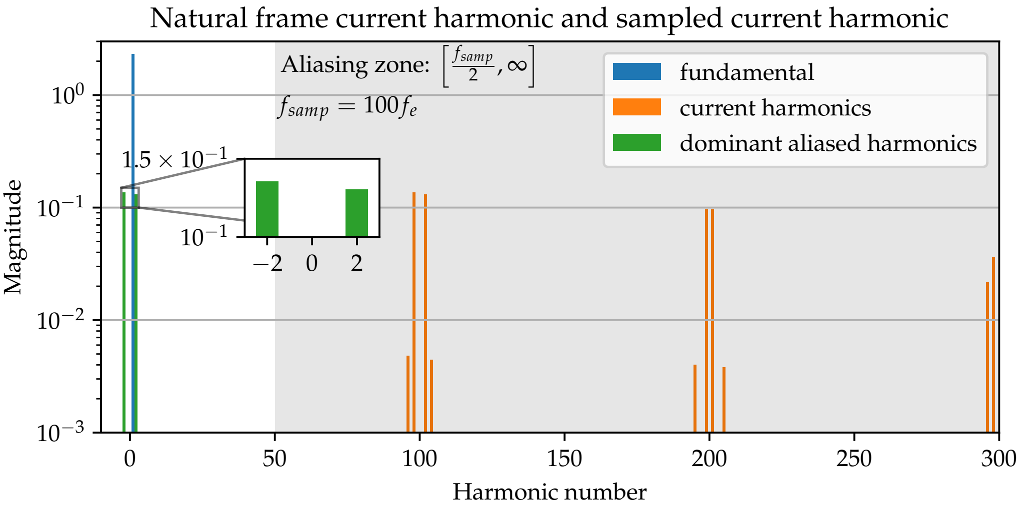

Figure 11. Natural frame current harmonics and dominant aliased current harmonics.

Let A_{n2} and A_{p2} be the magnitudes of the aforementioned two aliased harmonics. Taking into account the three-phase nature of the PMSM system, the aliased harmonics of PMSM can be expressed as follows:

$$\begin{cases} i_{a,\text{aliased}} = A_{n2}\cos(-4\pi f_e t - \phi_{an2}) + A_{p2}\cos(4\pi f_e t - \phi_{ap2}) \\ i_{b,\text{aliased}} = A_{n2}\cos\left(-4\pi f_e t - \phi_{bn2} - \frac{2\pi}{3}\right) + A_{p2}\cos\left(4\pi f_e t - \phi_{bp2} - \frac{2\pi}{3}\right) \\ i_{c,\text{aliased}} = A_{n2}\cos\left(-4\pi f_e t - \phi_{cn2} - \frac{4\pi}{3}\right) + A_{p2}\cos\left(4\pi f_e t - \phi_{cp2} - \frac{4\pi}{3}\right) \end{cases} \tag{25}$$

where $i_{a,\text{aliased}}$, $i_{b,\text{aliased}}$ and $i_{c,\text{aliased}}$ are the three dominant phase aliasing currents. In closed-loop control, these currents are fed back to the current controller, and even though these aliased currents do not exist in open-loop condition, the controller still takes them as an error and tries to compensate the aliased currents, which leads to real phase current harmonics at aliasing frequency.

The aliased current harmonics are then obtained by multiplying voltage harmonics (Equation (A9)) with the PMSM system transfer function gain on the δ axis:

$$\begin{cases} A_{n2} = \frac{2V_{DC}}{3\pi} J_{-2}\left(\frac{\pi}{2}D\right)|G_\delta(f_{sw} - 2f_e)| \\ A_{p2} = \frac{2V_{DC}}{3\pi} J_{2}\left(\frac{\pi}{2}D\right)|G_\delta(f_{sw} + 2f_e)| \end{cases} \tag{26}$$

Equation (25) shows the sum of two aliased currents from a three-phase point of view. The harmonic $n2$ is a sequence 2 component and the harmonic $p2$ is a sequence 1 component.

Equation (25) can be rewritten into sequence form using sequence vector representation:

$$\begin{cases} i_{a,\text{aliased}} = A_{p2}\cos(2\theta - \phi_{s1}) & + A_{n2}\cos(2\theta - \phi_{s2}) \\ i_{b,\text{aliased}} = A_{p2}\cos\left(2\theta - \phi_{s1} - \dfrac{2\pi}{3}\right) & + A_{n2}\cos\left(2\theta - \phi_{s2} - \dfrac{4\pi}{3}\right) \\ i_{c,\text{aliased}} = A_{p2}\cos\left(2\theta - \phi_{s1} - \dfrac{4\pi}{3}\right) & + A_{n2}\cos\left(2\theta - \phi_{s2} - \dfrac{2\pi}{3}\right) \end{cases} \tag{27}$$

According to the control strategy chosen by the system user, these aliased harmonics can be more or less disastrous, so the open-loop aliased harmonic magnitude is a reasonable reference for normalization. Let $A_{sp(CL)}$ and $A_{sn(CL)}$ be the sequence 1 and sequence 2 component at $2f$ in the phase current in closed-loop control and $phi_{sp(CL)}$, $phi_{sn(CL)}$ be their respective phase. Using the transfer formalism between phase current and DC-link current explained in Appendix A, the DC current ripple caused by the aliasing effect can be calculated.

$$\tilde{I}_{DC,\text{aliasing}} = \frac{3A_{sp(CL)}D\sin\left(\theta - \phi_{sp(CL)}\right)}{4} + \frac{3A_{np(CL)}D\sin\left(3\theta - \phi_{sn(CL)}\right)}{4} \tag{28}$$

It is worth noting that the sequence 2 component is the dominant component. Therefore, the DC ripple at three times fundamental frequency ($3f$) is greater than the DC ripple at $1f$ (fundamental frequency).

5.4. Simulation Results

Unlike other harmonics, the $3f$ harmonic in the DC-link current is due to ADC sampling that only exists in the closed-loop. Simulations in this section are performed in the closed-loop, first with only Σ control and then with Σ and δ control.

It can be found in Figure 12 that the $3f$ harmonic takes the most significant magnitude when there is a δ control and when the coupling factor k_n is big enough (HC winding). This phenomenon can be explained by the δ axis filter effect (Figure 10), and a more coupled winding results in less filtered high-frequency voltage harmonics from the PWM supply. Then, the high-frequency current harmonics are aliased into the bandwidth of the ADC, and the HC winding is more affected by aliased harmonics since its δ axis is not able to efficiently filter high-frequency harmonics. As demonstrated previously, those aliased current harmonics become harmonic $3f$ in the DC-link current. As for $1f$ DC current ripple, it is not visible in the chosen CRR display range of Figure 12. When no δ control is applied, the $3f$ harmonic is not visible in the simulation for the chosen current ripple ratio range.

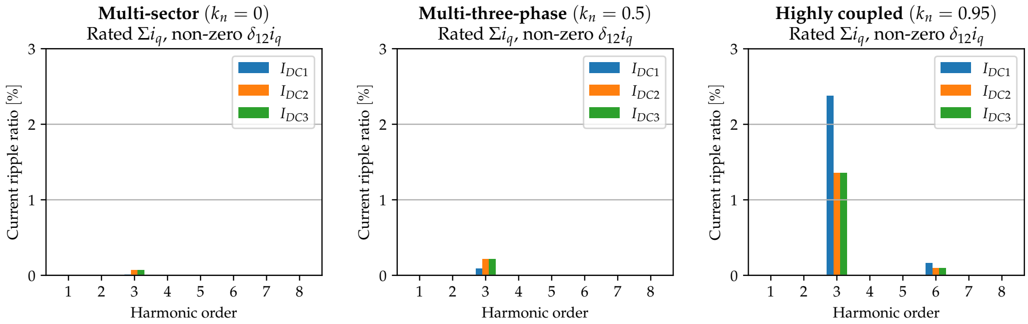

Figure 12. Closed-loop simulation results with ideal winding resistance, ideal inductance and ideal back-EMF. A zero-order hold is added to the current measurement simulating ADC sampling. Rated Σi_q at 18 A, $\delta_{12} i_q$ at -6 A, average DC current $\overline{I_{DC1}} = 0.8\,A$, $\overline{I_{DC2}} = \overline{I_{DC3}} = 3.8\,A$.

The simulation results confirm the analytical analysis. A direct comparison on $3f$ DC current ripple ratio between analytical model and simulation is not possible, because the closed-loop controller should be taken into account to make this comparison. Since this article's objective is not the controller design, the analysis only explains the existence of the $3f$ current ripple when using an ADC with the same sampling frequency as the inverter switching frequency.

6. Experimental and Simulation Results

The experimental setup of the HC winding multi-port PMSM drive is shown in Figure 13. The DC voltage source supplies three DC/AC inverters' DC-link at 48 V. Controlled by a MCU, namely the dSPACE MicroLabBox, the DC/AC inverters use the SPWM technique to supply the HC multi-port PMSM. The PMSM rotor shaft of PMSM is mechanically coupled to that of a DC permanent magnet (PM) generator, which serves as the mechanical load of motor drive. For this, load resistors are connected to the DC PM generator. The experimental parameters are similar to those of the simulation (Table 4).

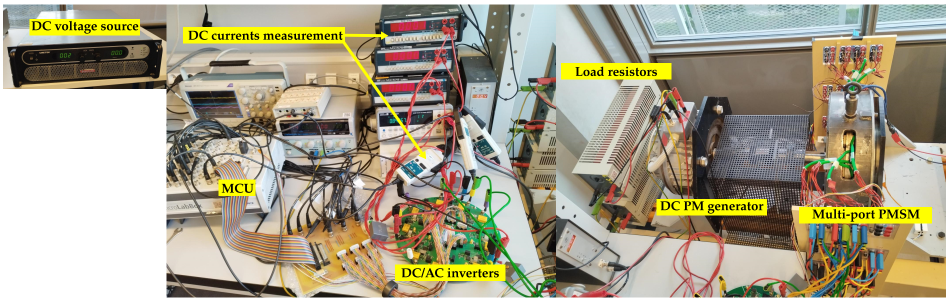

Figure 13. Experimental HC multi-port PMSM drive setup.

In Section 3–5, three types of harmonics have been identified, along with their respective cause. In a real motor drive, by the law of superposition, it is natural to find all three types of DC-link current harmonics. A DC current measurement result is presented in Figure 14: only the HC winding is realized (Figure 2b). Similarly to the simulation results, the current harmonic magnitudes are normalized with respect to the average of three DC-link current. The obtained normalized magnitude can be regarded as the current ripple ratio. In the experimental setup, the DC-link capacitors exist on the DC/AC inverter close to the switches, resulting in the low-frequency current harmonic filtered at the current measurement point. Since the studied frequency range is small ($2f$ to $6f$), the capacitor's filter effect is considered the same for all studied harmonics.

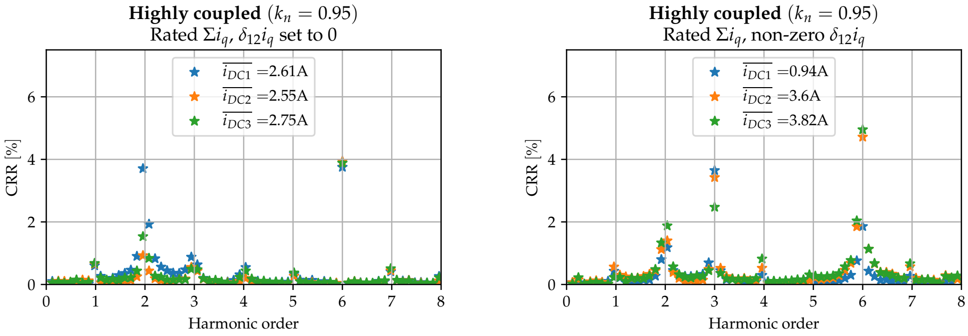

Figure 14. Experimental DC-link current measurement of a HC multi-port motor drive, with Σ control on the left (same DC currents for three sub-windings), with $\Sigma\delta$ control on the right (unequal DC currents).

In Figure 14, the harmonics $2f$ and $6f$ can be observed for both control references. The harmonic $3f$ only appears when the δ control is activated, because the PWM high-frequency voltage harmonics only alias significantly when δ reference is not 0. It can be observed that the maximum low-frequency DC-link ripple ratio of current harmonics is less than 5% in both control strategies.

Figure 15 presents simulation results performed in the closed-loop with measured resistance, inductance and back-EMF for three types of multi-port winding. For the HC winding configuration, the experimental measurement in Figure 14 and the simulation results in Figure 15 are compared in Table 5. Both results are consistent. The $2f$ and $6f$ harmonics exist in both control schemes, while the $3f$ harmonics have a significant value only when each of the three power sources have unequal power contributions. Indeed, the CRR of the $3f$ harmonics increases notably when an unequal effort is requested from each of the sources (due to a non-zero differential reference value). This result is revealed both in simulations and experiments. However, $2f$ harmonics are smaller in the experimental case than in the simulation case, possibly due to the uncertainty of the resistance and inductance measurements of the different windings. The $3f$ and $6f$ harmonics are larger in the experimental case, probably due to the lack of DC-link capacitor modeling and DC source modeling in the proposed approach.

Table 5. HC configuration: Comparison of the DC-link current ripple ratio (CRR) between the case of using equal contribution between the three sources and the case of dissimilar contribution from each source (non-zero differential reference value).

		Rated Σi_q $\delta_{12} i_q$ Set to 0			**Rated Σi_q Non-Zero $\delta_{12} i_q$**			**CRR Evolution Zero to Non-Zero $\delta_{12} i_q$**		
		I_{DC1}	I_{DC2}	I_{DC3}	I_{DC1}	I_{DC2}	I_{DC3}	I_{DC1}	I_{DC2}	I_{DC3}
Simulation	$2f$	4.9%	5.0%	5.1%	2.9%	5.4%	5.4%	−2.0%	+0.3%	+0.3%
	$3f$	0.2%	0.2%	0.2%	1.8%	0.9%	1.2%	+1.6%	+0.6%	+1.0%
	$6f$	2.1%	2.1%	2.1%	0.2%	2.9%	3.0%	−1.9%	+0.9%	+0.9%
Experiment	$2f$	3.7%	0.9%	1.5%	1.2%	1.4%	1.9%	−2.5%	+0.5%	+0.3%
	$3f$	0.9%	0.5%	0.5%	3.6%	3.4%	2.5%	+2.8%	+2.9%	+2.0%
	$6f$	3.8%	3.9%	3.9%	1.9%	4.7%	5.0%	−1.9%	+0.8%	+1.1%

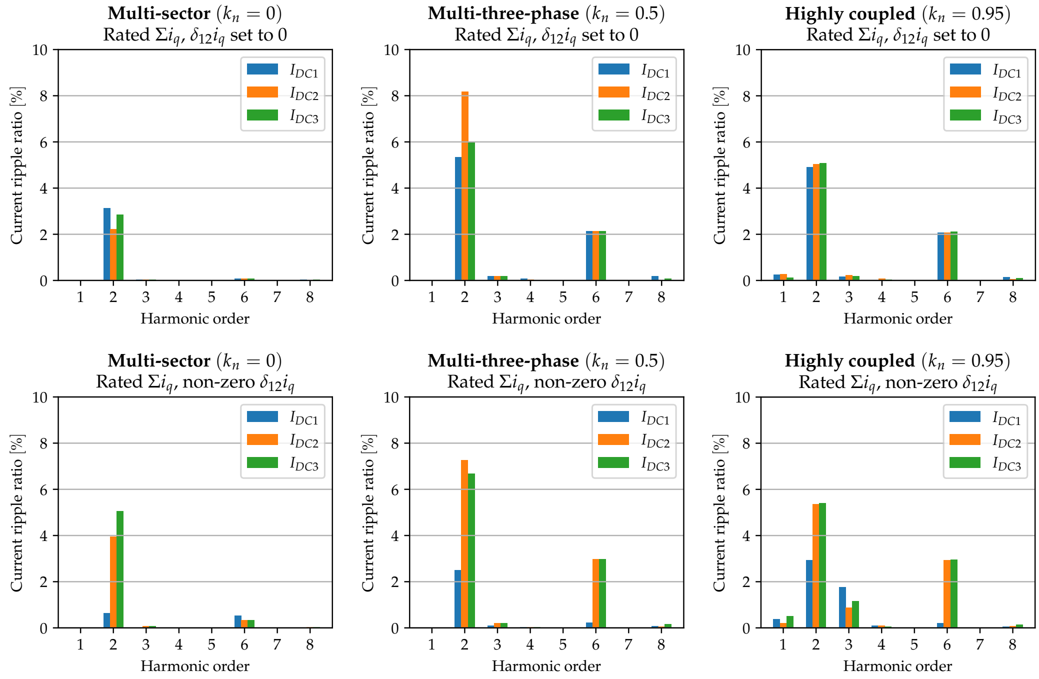

Figure 15. Simulations in closed-loop condition, with measured resistance, inductance matrix, back-EMF harmonics and ADC sampling. Rated Σi_q at 18 A, $\delta_{12} i_q$ at $-6\,A$. Average DC current $\overline{I_{DC1}} = \overline{I_{DC2}} = \overline{I_{DC3}} = 2.6\,A$ when no δ reference is set to 0. $\overline{I_{DC1}} = 0.8\,A$ $\overline{I_{DC2}} = \overline{I_{DC3}} = 3.7\,A$ when δ reference is non-zero.

Figure 16 compares the experimental waveform of Figure 14 and the simulation waveform of Figure 15 for the HC winding. An ideal low-pass filter is applied to the simulation waveform in order to highlight the low-frequency harmonics. The two waveforms exhibit a similar average current at the same current reference, while the ripple component in the experiment is visibly higher than that in the simulation. It is because the DC-link capacitor is unable to fully filter high-frequency harmonics induced by inverter switching. In the low-frequency range, the current harmonics are even more poorly filtered and are therefore visible in the experimental waveform.

The results of this study gave the following data for the studied synchronous machine, segmented into three elementary submachines according to three different processes, namely the MS, P-3ph and HC architectures. In the open-loop and compared to the studied PMSM, an unbalanced winding causes the highest current ripple rate of 15% in a strongly coupled winding, while the MS presents only 6%. In the presence of back-EMF harmonics, all three segmentation types exhibit the same current ripple rate of 1%. In closed-loop, and with unequal contributions from the power DC sources, the HC configuration has the highest current ripple rate of 2.5%, while the current ripple rate for the MS one is negligible. However, the current ripple rate for all three closed-loop winding structures is less than 15%, which is considered acceptable for motor control applications.

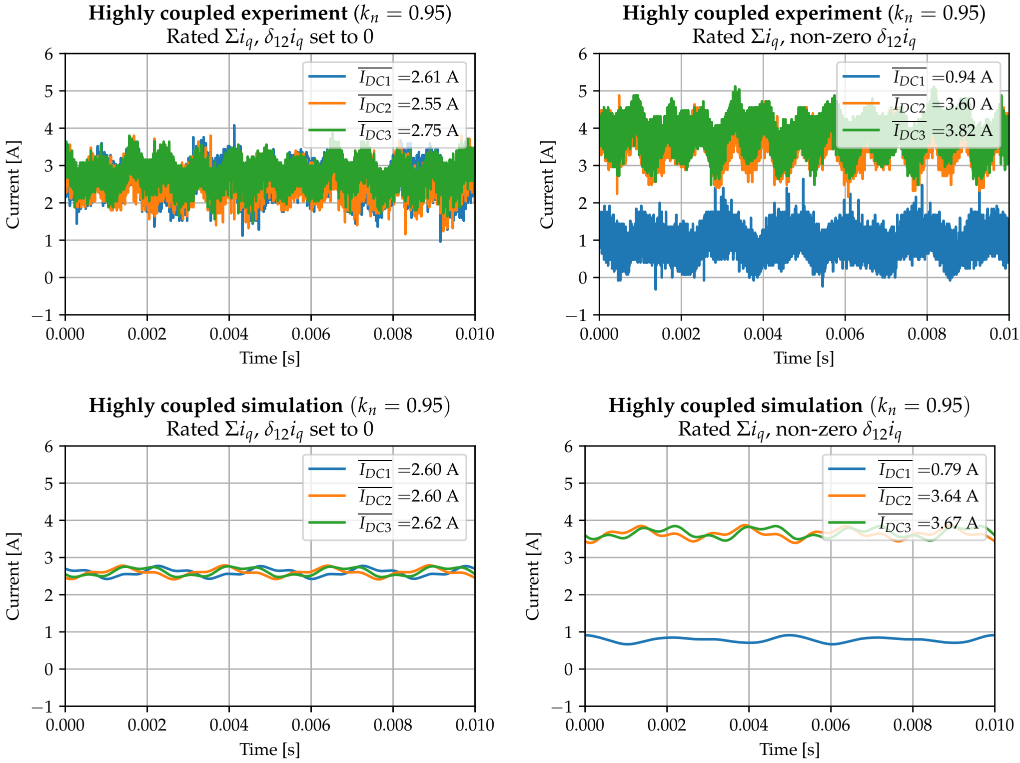

Figure 16. Waveform of the HC winding in a closed-loop experiment (**top**) and simulation (**bottom**). The experimental and simulated conditions are the same as depicted in Figures 14 and 15.

7. Conclusions

The work presented in this article provides a detailed analysis of the possible DC-link current low-frequency harmonics in multi-port motor drives using symmetrical sequence formalism. Specifically focusing on three harmonics ($2f, 3f, 6f$), their analytical expressions are derived and simulations are conducted to validate the analytical results. Additionally, experiments are carried out for HC winding motor drives, demonstrating good agreement with the analytical and simulation results.

A comparison among three multi-port PMSM structures suitable for power-sharing applications reveals that the harmonic magnitudes exhibit similar trends with the coupling factor between sub-windings: the MS structure exhibits the least $2f$ and $3f$ harmonics.

The impact of power sharing on the DC-link current harmonics is also analyzed. In the suggested $\Sigma\delta$ control scheme, power-sharing involves activating the δ axis control. For multi-port winding structures with a high coupling factor between sub-windings, the δ axis transfer function has a wide bandwidth, which may lead to unfiltered high-frequency current harmonics aliasing to low-frequency harmonics. Under the studied conditions where the sampling frequency is the same as the switching frequency, a dominant $3f$ harmonic appears in the DC-link current.

Furthermore, it is found that the three studied harmonics have very limited impact on the quality of the DC current, with an average ripple ratio of only 15%.

According to the application, the DC-link current ripple requirement varies. If a minimum low-frequency DC current ripple is expected, the following design rules should be followed:

- Avoid winding unbalance in the multi-port PMSM manufacturing phase. If unbalance is inevitable, choose a less coupled winding configuration, such as the MS winding one.
- Add an anti-aliasing filter between the current sensor and the ADC, in order to filter the sideband harmonics at switching frequency and its multiples [34,35].
- Choose a winding configuration with the most sinusoidal back-EMF, or apply the skew technique on the stator or rotor [41,42], or use online-trained ADAptive LInear NEuron (ADALINE) to mitigate the induced harmonic [43].

In future works, the impact of current harmonics on the lifespan of voltage sources should be investigated. If the impact is significant, possible solutions for mitigating these low-frequency DC-link current harmonics should be studied. Potential solutions may include the design of a well-tailored control strategy (e.g. ADALINE and H_∞ control) and the implementation of an anti-aliasing filter.

Author Contributions: Conceptualization, Y.L., A.C., A.V., J.O. and O.B.; data curation, Y.L.; formal analysis, Y.L.; investigation, Y.L.; methodology, Y.L., A.C., A.V., J.O. and O.B.; software, Y.L.; supervision, A.C., A.V., J.O. and O.B.; validation, A.C., A.V., J.O. and O.B.; visualization, Y.L.; writing—original draft, Y.L.; writing—review and editing, Y.L., A.C., A.V., J.O. and O.B. All authors have read and agreed to the published version of the manuscript.

Funding: This research received no external funding.

Data Availability Statement: Data will be made available on request.

Conflicts of Interest: The authors declare no conflicts of interest.

Abbreviations

The following abbreviations are used in this manuscript:

ADC	Analog-to-Digital converter
CL	Closed-loop
CRR	Current ripple ratio
Back-EMF	Counter-electromotive force
HC	Highly coupled
MCU	Multipoint control unit
MMF	Magnetomotive force
MS	Multi-sector
OL	Open-loop
PEMFC	Proton exchange membrane fuel cell
PM	Permanent magnet
PMSM	Permanent magnet synchronous motor
P-3ph	Multi-three-phase
RMS	Root mean square

SPWM	Sinusoidal pulse width modulation
VSI	Voltage source inverter
$2f$	Twice fundamental frequency
$3f$	Three times fundamental frequency
$5f$	Five times fundamental frequency
$6f$	Six times fundamental frequency
$7f$	Seven times fundamental frequency

Appendix A. Average DC Current Calculation Formalism

A sinusoidal AC voltage or current can be represented as a vector using its magnitude and phase. For instance, $A\sin(\theta+\phi)$ becomes $Ae^{j\angle(\theta+\phi)}$, denoting a vector with a length of $|A|$ and an angle of $\theta+\phi$, with $0°$ serving as the phase reference.

A general expression for an unbalanced three-phase current under balanced voltage supply is proposed as follows:

$$\begin{cases} V_a = \hat{V}\sin(\theta) \\ V_b = \hat{V}\sin\left(\theta - \dfrac{2\pi}{3}\right) \\ V_c = \hat{V}\sin\left(\theta - \dfrac{4\pi}{3}\right) \end{cases} \quad \begin{cases} I_a = \hat{I}_a\sin(\theta - \phi_a) \\ I_b = \hat{I}_b\sin\left(\theta - \phi_b - \dfrac{2\pi}{3}\right) \\ I_c = \hat{I}_c\sin\left(\theta - \phi_c - \dfrac{4\pi}{3}\right) \end{cases} \tag{A1}$$

where each phase has its own magnitude and phase delay. According to [19], the unbalanced three-phase current can be expressed as the sum of sequence 1 and sequence 2 current vectors, assuming no 0 sequence current exists in the three-phase system. The magnitude and phase of these two sequences can be determined using phasor transformation, which is defined as

$$\begin{pmatrix} \underline{I_0} \\ \underline{I_1} \\ \underline{I_2} \end{pmatrix} = \frac{1}{3}\begin{bmatrix} 1 & 1 & 1 \\ 1 & \omega_3 & \omega_3^2 \\ 1 & \omega_3^2 & \omega_3 \end{bmatrix}\begin{pmatrix} \underline{I_a} \\ \underline{I_b} \\ \underline{I_c} \end{pmatrix} \tag{A2}$$

where ω_3 is the phasor operator, which is equivalent to $e^{j2\pi/3}$ and signifies a positive rotation of $2\pi/3$ in vector operations. $\underline{I_a}$, $\underline{I_b}$, and $\underline{I_c}$ are three vectors representing the three-phase unbalanced current, with $\underline{V_a}$ serving as the phase reference. Similarly, $\underline{I_0}$, $\underline{I_1}$, and $\underline{I_2}$ are three vectors representing the 0 sequence, sequence 1, and sequence 2 current, respectively.

In Figure A1a, an example of unbalanced three-phase currents without 0 sequence component is illustrated. After the transformation (A2), sequence 1 $\underline{I_1}$ and sequence 2 $\underline{I_2}$ vectors are obtained, as shown in Figure A1b. These two sequence vectors can help reconstruct the initial three-phase currents using the following form:

$$\begin{cases} I_a = |\underline{I_1}|\sin(\theta + \angle\underline{I_1}) + |\underline{I_2}|\sin(\theta + \angle\underline{I_2}) \\ I_b = |\underline{I_1}|\sin\left(\theta + \angle\underline{I_1} - \dfrac{2\pi}{3}\right) + |\underline{I_2}|\sin\left(\theta + \angle\underline{I_2} - \dfrac{4\pi}{3}\right) \\ I_c = |\underline{I_1}|\sin\left(\theta + \angle\underline{I_1} - \dfrac{4\pi}{3}\right) + |\underline{I_2}|\sin\left(\theta + \angle\underline{I_2} - \dfrac{2\pi}{3}\right) \end{cases} \tag{A3}$$

In an electrical period, 6 zones are identified: A, B, C, D, E, and F, in each zone, the order of three voltage references stays the same (Figure A2). For example, in zone A, the following relation is verified: $v_a > v_c > v_b$.

The DC current is obtained from the switching function S, since the following relation exists between phase current and the DC-link current:

$$i_{dc} = S_{Q1}i_a + S_{Q3}i_b + S_{Q5}i_c \tag{A4}$$

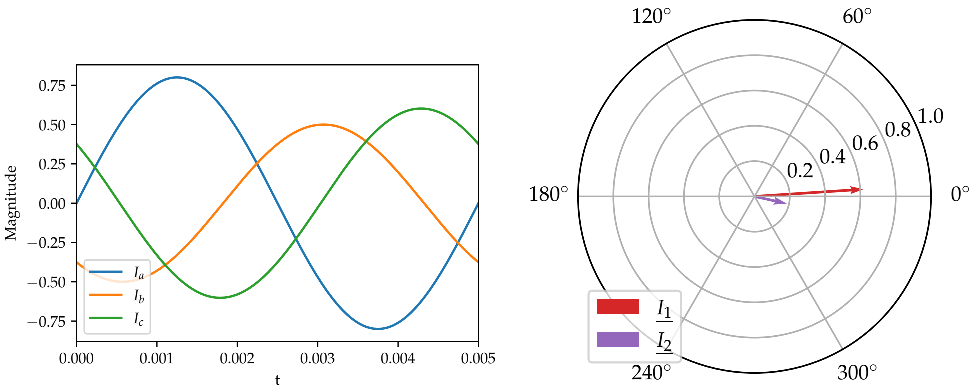

(**a**) (**b**)

Figure A1. Transformation between unbalanced three-phase current and sequence vectors. (**a**) An example of unbalanced three-phase currents. (**b**) Sequence vectors.

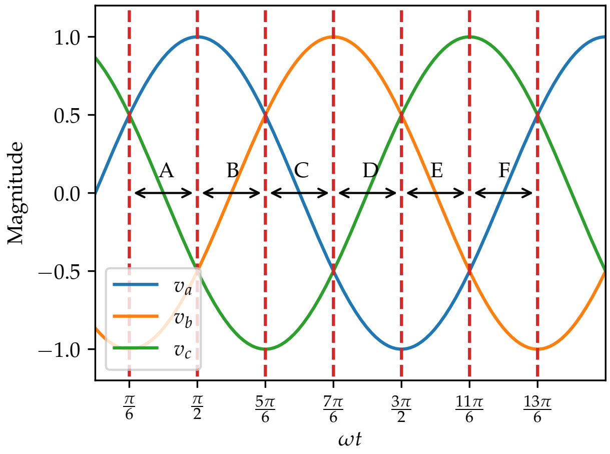

Figure A2. Open-loop three phase voltage references.

Besides, the length of every switching interval (T_0,T_1,T_2,T_3) can be calculated using the expression of SPWM reference (Figure A3):

$$\begin{cases} T_0 = \dfrac{T_s}{4}(1 - D\sin\theta) \\ T_1 = \dfrac{T_s}{4}D\left[\sin\theta - \sin\left(\theta - \dfrac{4\pi}{3}\right)\right] \\ T_2 = \dfrac{T_s}{4}D\left[\sin\left(\theta - \dfrac{4\pi}{3}\right) - \sin\left(\theta - \dfrac{2\pi}{3}\right)\right] \\ T_3 = \dfrac{T_s}{4}\left[1 + D\sin\left(\theta - \dfrac{2\pi}{3}\right)\right] \end{cases} \tag{A5}$$

with D the modulation depth of SPWM.

The average DC-link current for zone A is obtained by integrating the DC current over each switching interval:

$$\begin{aligned} I_{DC} &= \frac{1}{T_s}\int_{t_0}^{t_0+T_s} i_{dc}\mathrm{d}t \\ &= \frac{3D|\underline{I_1}|\cos\angle\underline{I_1}}{4} - \frac{3D|\underline{I_2}|\cos(2\theta + \angle\underline{I_2})}{4} \end{aligned} \tag{A6}$$

where t_0 is the start time of a switching period. Using the same approach for zone B to zone F, the same result as Equation (A6) can be obtained.

Equation (A6) demonstrates that unbalanced three-phase currents in a DC/AC inverter lead to DC current ripple with twice the electrical frequency. If no unbalance exists, $\underline{I}_2 = 0$.

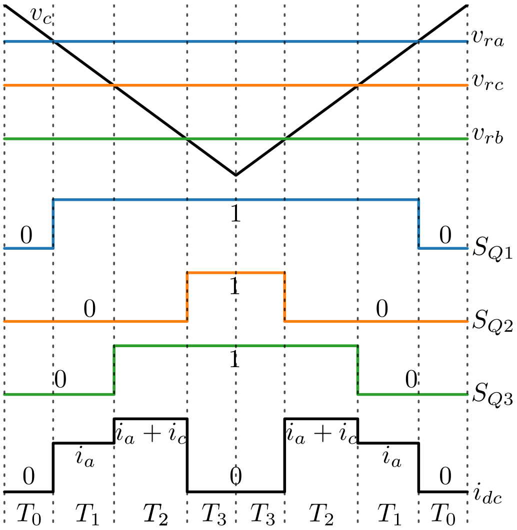

Figure A3. Inside a switching period for zone A: relations between PWM references, switching functions and DC-link current for the conventional three-phase DC/AC inverter case.

The expression obtained in Equation (A6) is the average DC current value during a switching period, but this is not accurate enough to reflect the DC capacitor current stress, because the high-frequency ripple is not taken into account. However, this expression is enough to describe the low-frequency current ripple, since the switching frequency is much greater than the analyzed frequency range.

Appendix B. Voltage Harmonics of SPWM Supplied 3-Wire-Y-Connected Load

A widely accepted PWM load voltage analytical expression is proposed in [40] for half-bridge single phase DC/AC voltage source inverter (VSI), for the naturally sampled sin-triangle modulation case, the load voltage is expressed as follows using double Fourier series:

$$\begin{aligned} v_L = & \frac{V_{DC}D}{2}\cos(\omega_o t + \phi_o) \\ & \boxed{\text{fundamental}} \\ & + \frac{2V_{DC}}{\pi}\sum_{m=1}^{\infty}\frac{1}{m}J_0\left(m\frac{\pi}{2}D\right)\sin\left(m\frac{\pi}{2}\right)\cos[m(\omega_c t + \phi_c)] \\ & \qquad\qquad \boxed{\text{carrier harmonics}} \\ & + \frac{2V_{DC}}{\pi}\sum_{m=1}^{\infty}\sum_{\substack{n=-\infty \\ (n\neq 0)}}^{\infty}\frac{1}{m}J_n\left(m\frac{\pi}{2}D\right)\sin\left[(m+n)\frac{\pi}{2}\right]\cos[m(\omega_c t + \phi_c) + n(\omega_o t + \phi_o)] \\ & \qquad\qquad\qquad\qquad \boxed{\text{sideband harmonics}} \end{aligned} \tag{A7}$$

where ω_o and ϕ_o are reference angular speed and initial phase, ω_c and ϕ_c are carrier angular speed and initial phase, J_n is the Bessel function of order n.

In Figure A4, structure of half-bridge single-phase VSI and three-phase VSI are illustrated. The three-phase DC/AC VSI can then be considered as three single phase DC/AC VSI, where a $2\pi/3$ phase delay is applied between each two references. Therefore, v_{az}, v_{bz} and v_{cz} can be calculated using Equation (A7).

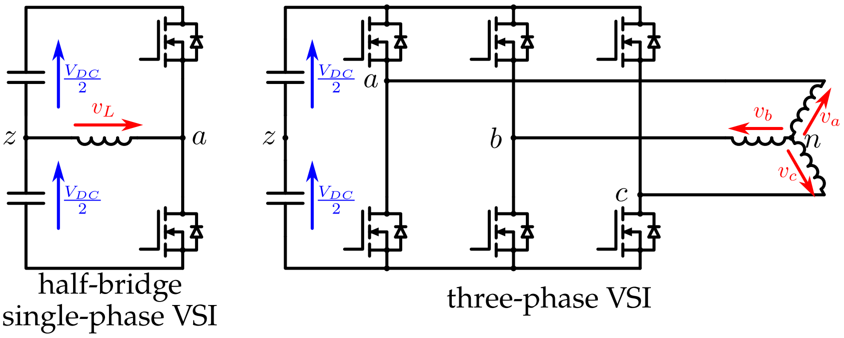

Figure A4. Load voltage of single-phase and three-phase DC/AC inverters.

In a three-phase VSI, the following voltage relations exist:

$$\begin{cases} v_a = \frac{1}{3}(2v_{az} - v_{bz} - v_{cz}) \\ v_b = \frac{1}{3}(2v_{bz} - v_{az} - v_{cz}) \\ v_c = \frac{1}{3}(2v_{cz} - v_{az} - v_{bz}) \end{cases} \tag{A8}$$

From Equations (A7) and (A8), the phase voltage of the double Fourier series of the three-phase VSI can be deducted. For example, v_a is expressed as follows:

$$\begin{aligned} v_a = & \underbrace{\frac{V_{DC}D}{2}\cos(\omega_o t + \phi_o)}_{\boxed{\text{fundamental}}} \\ & + \frac{2V_{DC}}{3\pi}\sum_{m=1}^{\infty}\sum_{\substack{n=-\infty \\ (n\neq 0)}}^{\infty}\frac{1}{m}J_n\left(m\frac{\pi}{2}D\right)\sin\left[(m+n)\frac{\pi}{2}\right] \\ & \times\left\{2\cos[m(\omega_c t + \phi_c) + n(\omega_o t + \phi_o)] - \cos\left[m(\omega_c t + \phi_c) + n(\omega_o t + \phi_o - \frac{2\pi}{3})\right]\right. \\ & \left.- \cos\left[m(\omega_c t + \phi_c) + n(\omega_o t + \phi_o - \frac{4\pi}{3})\right]\right\} \\ & \boxed{\text{sideband harmonics}} \end{aligned} \tag{A9}$$

In the three-phase system, voltage carrier harmonics cancel out because there is no phase delay between three carriers, and it only remains the fundamental component and sideband harmonics.

References

1. Sala, G.; Valente, G.; Nardo, M.D.; Degano, M.; Zanchetta, P.; Gerada, C. Power-Sharing Control in Bearingless Multi-Sector and Multi-Three-Phase Permanent Magnet Machines. *IEEE Trans. Ind. Electron.* **2021**, *68*, 9070–9080. [CrossRef]
2. Wen, Z.; Nardo, M.D.; Sala, G.; Valente, G.; Marfoli, A.; Degano, M.; Zanchetta, P.; Gerada, C. Modular Power Sharing Control for Bearingless Multithree Phase Permanent Magnet Synchronous Machine. *IEEE Trans. Ind. Electron.* **2022**, *69*, 6600–6610. [CrossRef]
3. Abdel-Khalik, A.S.; Massoud, A.; Ahmed, S. Standard Three-Phase Stator Frames for Multiphase Machines of Prime-Phase Order: Optimal Selection of Slot/Pole Combination. *IEEE Access* **2019**, *7*, 78239–78259. [CrossRef]
4. Hua, H.; Chen, H.; Hua, W. Comparative Investigation of Dual Three-Phase Permanent Magnet Synchronous Machines With Different Winding Configurations. *IEEE Trans. Ind. Appl.* **2024**, *60*, 3120–3130. [CrossRef]
5. Rubino, S.; Dordevic, O.; Bojoi, R.; Levi, E. Modular Vector Control of Multi-Three-Phase Permanent Magnet Synchronous Motors. *IEEE Trans. Ind. Electron.* **2021**, *68*, 9136–9147. [CrossRef]
6. Hoang, E.; Laboure, E. Electric Machine Supplied at Low Voltage and Associated Multicellular Power Train. U.S. Patent 10985626B2, 20 April 2021.
7. Cizeron, A.; Ojeda, J.; Monmasson, E.; Bethoux, O. Control of a Segmented Three-Phase Synchronous Motor with Highly Coupled Sub-Windings. *IEEE Trans. Ind. Electron.* **2022**, *70*, 4405–4415. [CrossRef]

8. Zhang, Q.; Raherimihaja, H.J.; Xu, G.; Zhang, X. Design and Performance Analysis of Segmented Three-Phase IPMSM for EVs Integrated Battery Charger. *IEEE Trans. Ind. Electron.* **2021**, *68*, 9114–9124. [CrossRef]
9. Zhang, W.; Xu, Y.; Huang, H.; Zou, J. Vibration Reduction for Dual-Branch Three-Phase Permanent Magnet Synchronous Motor With Carrier Phase-Shift Technique. *IEEE Trans. Power Electron.* **2020**, *35*, 607–618. [CrossRef]
10. Kieferndorf, F.; Forster, M.; Lipo, T. Reduction of DC-bus capacitor ripple current with PAM/PWM converter. *IEEE Trans. Ind. Appl.* **2004**, *40*, 607–614. [CrossRef]
11. Dahono, P.; Sato, Y.; Kataoka, T. Analysis and minimization of ripple components of input current and voltage of PWM inverters. *IEEE Trans. Ind. Appl.* **1996**, *32*, 945–950. [CrossRef]
12. Guo, C.; Xin, Z.; Han, J.; Hu, L.; Lu, B. Review of the calculation of DC-link capacitor current. *Front. Energy Res.* **2023**, *11*, 1240755. [CrossRef]
13. Guo, J.; Ye, J.; Emadi, A. DC-Link Current and Voltage Ripple Analysis Considering Antiparallel Diode Reverse Recovery in Voltage Source Inverters. *IEEE Trans. Power Electron.* **2018**, *33*, 5171–5180. [CrossRef]
14. Safayet, A.; Islam, M.; Sebastian, T. Comprehensive Analysis for DC-Link Capacitor Sizing for a Three-Phase Current-Controlled Voltage-Source Inverter. *IEEE Trans. Ind. Appl.* **2022**, *58*, 4248–4260. [CrossRef]
15. Wang, T.; Lu, S. Dc-link current computational methods for three-phase inverter with low-order harmonic output current. *Iet Power Electron.* **2019**, *12*, 878–890. [CrossRef]
16. Kolar, J.; Wolbank, T.; Schrodl, M. Analytical calculation of the RMS current stress on the DC link capacitor of voltage DC link PWM converter systems. In Proceedings of the 1999 Ninth International Conference on Electrical Machines and Drives (Conf. Publ. No. 468), Canterbury, UK, 1–3 September 1999; pp. 81–89. [CrossRef]
17. Taha, W.; Azer, P.; Poorfakhraei, A.; Dhale, S.; Emadi, A. Comprehensive Analysis and Evaluation of DC-Link Voltage and Current Ripples in Symmetric and Asymmetric Two-Level Six-Phase Voltage Source Inverters. *IEEE Trans. Power Electron.* **2023**, *38*, 2215–2229. [CrossRef]
18. Verkroost, L.; Van Damme, J.; Bozalakov, D.V.; De Belie, F.; Sergeant, P.; Vansompel, H. Simultaneous DC-Link and Stator Current Ripple Reduction With Interleaved Carriers in Multiphase Controlled Integrated Modular Motor Drives. *IEEE Trans. Ind. Electron.* **2021**, *68*, 5616–5625. [CrossRef]
19. Pei, X.; Zhou, W.; Kang, Y. Analysis and Calculation of DC-Link Current and Voltage Ripples for Three-Phase Inverter With Unbalanced Load. *IEEE Trans. Power Electron.* **2015**, *30*, 5401–5412. [CrossRef]
20. Vujacic, M.; Dordevic, O.; Mandrioli, R.; Grandi, G. DC-link low-frequency current and voltage ripple analysis in multiphase voltage source inverters with unbalanced load. *IET Electr. Power Appl.* **2022**, *16*, 300–314. [CrossRef]
21. Baburajan, S.; Wang, H.; Mandrile, F.; Yao, B.; Wang, Q.; Kumar, D.; Blaabjerg, F. Design of Common DC-Link Capacitor in Multiple-Drive System Based on Reduced DC-Link Current Harmonics Modulation. *IEEE Trans. Power Electron.* **2022**, *37*, 9703–9717. [CrossRef]
22. Chen, T.; Li, S.; Fahimi, B. Analysis of DC-Link Voltage Ripple in Voltage Source Inverters without Electrolytic Capacitor. In Proceedings of the IECON 2018—44th Annual Conference of the IEEE Industrial Electronics Society, Washington, DC, USA, 21–23 October 2018; pp. 1041–1048. [CrossRef]
23. Gao, R.; Wang, G.; Zhang, G.; Ren, Z.; Xu, D. Active Damping Control Strategy With Power Analysis for Reduced DC-Link Capacitance PMSM Drives. In Proceedings of the 2022 IEEE 31st International Symposium on Industrial Electronics (ISIE), Anchorage, AK, USA, 1–3 June 2022; pp. 468–473. [CrossRef]
24. Bessman, A.; Soares, R.; Wallmark, O.; Svens, P.; Lindbergh, G. Aging effects of AC harmonics on lithium-ion cells. *J. Energy Storage* **2019**, *21*, 741–749. [CrossRef]
25. Ghassemi, A.; Banerjee, P.C.; Zhang, Z.; Hollenkamp, A.; Bahrani, B. Aging Effects of Twice Line Frequency Ripple on Lithium Iron Phosphate (LiFePO4) Batteries. In Proceedings of the 2019 21st European Conference on Power Electronics and Applications (EPE '19 ECCE Europe), Genova, Italy, 3–5 September 2019; pp. P.1–P.9. [CrossRef]
26. Brand, M.J.; Hofmann, M.H.; Schuster, S.S.; Keil, P.; Jossen, A. The Influence of Current Ripples on the Lifetime of Lithium-Ion Batteries. *IEEE Trans. Veh. Technol.* **2018**, *67*, 10438–10445. [CrossRef]
27. Ghassemi, A.; Chakraborty Banerjee, P.; Hollenkamp, A.F.; Zhang, Z.; Bahrani, B. Effects of alternating current on Li-ion battery performance: Monitoring degradative processes with in-situ characterization techniques. *Appl. Energy* **2021**, *284*, 116192. [CrossRef]
28. Guilbert, D.; N'Diaye, A.; Luberda, P.; Djerdir, A. Fuel Cell Lifespan Optimization by Developing a Power Switch Fault-Tolerant Control in a Floating Interleaved Boost Converter. *Fuel Cells* **2017**, *17*, 196–209.[CrossRef]
29. Choi, W.; Howze, J.W.; Enjeti, P. Development of an equivalent circuit model of a fuel cell to evaluate the effects of inverter ripple current. *J. Power Sources* **2006**, *158*, 1324–1332. [CrossRef]
30. Mariscotti, A. Power Quality Phenomena, Standards, and Proposed Metrics for DC Grids. *Energies* **2021**, *14*, 6453. [CrossRef]
31. Demir, Y.; EL-Refaie, A.M.; Aydin, M. Investigation of Asymmetric and Unbalanced Winding Structures for 3-Phase Permanent Magnet Synchronous Machines. *IEEE Trans. Energy Convers.* **2021**, *36*, 1722–1732. [CrossRef]
32. Basnet, B.; Aljehaimi, A.M.; Pillay, P. Back-EMF Analysis of a Variable Flux Machine for Different Magnetization States. *IEEE Trans. Ind. Electron.* **2021**, *68*, 9125–9135. [CrossRef]
33. Ren, X.; Li, D.; Qu, R.; Pei, T. Back EMF Harmonic Analysis of Permanent Magnet Magnetic Geared Machine. *IEEE Trans. Ind. Electron.* **2020**, *67*, 6248–6258. [CrossRef]

34. Geng, H.; Xu, Y.; Wu, W. Aliasing Suppression Method for a Three-Phase Grid-Connected Photovoltaic Inverter Based on Multi-Sampling and Mean Filtering. *Energies* **2024**, *17*, 907. [CrossRef]
35. He, S.; Zhou, D.; Wang, X.; Blaabjerg, F. Aliasing Suppression of Multisampled Current-Controlled LCL-Filtered Inverters. *IEEE J. Emerg. Sel. Top. Power Electron.* **2022**, *10*, 2411–2423. [CrossRef]
36. Semail, E.; Bouscayrol, A.; Hautier, J.P. Vectorial formalism for analysis and design of polyphase synchronous machines. *Eur. Phys. J. Appl. Phys.* **2003**, *22*, 207–220. [CrossRef]
37. Jiang, D.; Liu, K.; Liu, Z.; Wang, Q.; He, Z.; Qu, R. Four-Module Three-Phase PMSM Drive for Suppressing Vibration and Common-Mode Current. *IEEE Trans. Ind. Appl.* **2021**, *57*, 4874–4883. [CrossRef]
38. Hu, Y.; Zhu, Z.Q.; Odavic, M. Comparison of Two-Individual Current Control and Vector Space Decomposition Control for Dual Three-Phase PMSM. *IEEE Trans. Ind. Appl.* **2017**, *53*, 4483–4492. [CrossRef]
39. Hsu, H.H.; Tzou, Y.Y. FPGA control and implementation of a multiphase-interleaved PWM inverter for a segmented PMSM. In Proceedings of the 2015 IEEE 11th International Conference on Power Electronics and Drive Systems, Sydney, Australia, 9–12 June 2015; pp. 224–230. [CrossRef]
40. Grahame, H.D. *Pulse Width Modulation for Power Converters: Principles and Practice*; IEEE Press Series on Power Engineering; Wiley-IEEE Press: Hoboken, NJ, USA, 2003.
41. Cawkwell, T.; Haris, A.; Gonzalez, J.M.; Rodrigues, L.K.; Shirokov, V. A Methodology for Applying Skew in an Automotive Interior Permanent Magnet Rotor for Robust Electromagnetic and Noise, Vibration and Harshness Performance. *World Electr. Veh. J.* **2023**, *14*, 350. [CrossRef]
42. Ji, S.; Li, Y.; Ou, H.; Tian, W. Design Principles and Calculation Criteria for Skewed Notches in PM Motors. *Energies* **2023**, *16*, 3783. [CrossRef]
43. Vu, D.T.; Nguyen, N.K.; Semail, E. Fault-Tolerant Control for Nonsinusoidal Multiphase Drives with Minimum Torque Ripple. *IEEE Trans. Power Electron.* **2022**, *37*, 6290–6304. [CrossRef]